Joule

CellPress
OPEN ACCESS

Article

Electrified thermochemical reaction systems with high-frequency metamaterial reactors

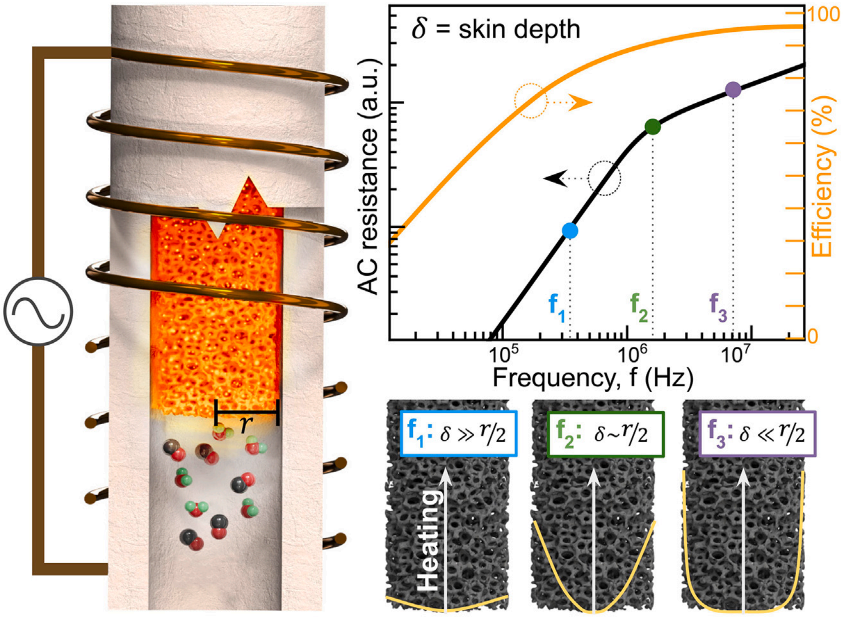

We introduce metamaterial reactors that leverage high-frequency magnetic induction for enhanced electrified thermochemical processing. Co-design of the reactor baffle properties with power electronics enables volumetric heating with near-unity heating efficiencies. The concept supports a clear pathway for scale-up and process intensification, thereby serving as a potential platform for decarbonized chemical reforming at industrially relevant scales.

Calvin H. Lin, Chenghao Wan, Zhennan Ru, ..., Matthew W. Kanan, Juan Rivas-Davila, Jonathan A. Fan

jonfan@stanford.edu

Highlights

A metamaterial reactor powered using high-frequency magnetic induction is implemented

Volumetric heating is realized by metamaterial baffle and power electronics co-design

The conversion efficiency of electricity to internal reactor heat is over 85%

Near-equilibrium conversion of the reverse water-gas shift reaction is demonstrated

Lin et al., Joule *8*, 2938–2949
October 16, 2024
Published by Elsevier Inc.
https://doi.org/10.1016/j.joule.2024.07.017

CellPress
OPEN ACCESS

Joule

Article

Electrified thermochemical reaction systems with high-frequency metamaterial reactors

Calvin H. Lin,[1,5] Chenghao Wan,[1,5] Zhennan Ru,[2] Connor Cremers,[1] Pinak Mohapatra,[1] Dolly L. Mantle,[3] Kesha Tamakuwala,[4] Ariana B. Höfelmann,[1] Matthew W. Kanan,[4] Juan Rivas-Davila,[1] and Jonathan A. Fan[1,6,*]

SUMMARY

We present metamaterial reactors as an innovative class of electrified thermochemical reactors that utilize high-frequency magnetic induction of an open-lattice metamaterial baffle to generate volumetric heat. A central design feature is the modeling of the metamaterial as an effective electrically conducting medium, abstracting its detailed microscopic geometry to a macroscopic susceptor description suitable for reactor-scale electromagnetic characterization. Co-design of the power electronics with the metamaterial provides design rules for efficient and volumetric heating, including the requirement for high induction frequencies. We implement lab-scale reactors with ceramic metamaterial baffles (39 mm in diameter) and megahertz-frequency power amplifiers to perform the reverse water-gas shift reaction, demonstrating reactor operation with near-unity heating efficiencies and radially uniform heating profiles. These clean energy concepts provide a broader context for structured reactors in which volumetric internal heating and complementary reaction engineering properties are collectively tailored to enable ideal operation regimes.

INTRODUCTION

The chemicals industry is a challenging sector to decarbonize due to its need of high-grade heat for thermochemical processing, which is conventionally and economically produced through the combustion of fossil fuels.[1] For many endothermic reactions, high reactor temperatures (i.e., hundreds of degrees Celsius) are required to enable reactor operating regimes featuring high conversion and enhanced kinetics. To this end, innovations in industrial decarbonization have been proposed in which green electricity is utilized to drive chemical reactions with reduced carbon intensity.[2,3] The innovations are manifold and range from breakthroughs in electrochemical catalysis and electrolyzer technologies[4,5] to the accessing of non-thermal equilibrium chemical pathways via hot electron phenomena[6] and transient heating.[7]

Although many of these concepts are promising, the most immediately translatable industrial decarbonization solutions utilize green electricity to drive steady-state thermochemical processes toward optimal reactant conversions.[8] These concepts can readily extend to industrial-scale chemical production, and they take advantage of a mature catalyst chemistry and manufacturing ecosystem. They can further enable innovative regimes of process intensification and streamlining of process systems for heat generation because they offer fundamentally different ways of transferring heat into the reactor compared with conventional methods based on

CONTEXT & SCALE

The chemical industry is challenging to decarbonize because of its need for high-grade heat, which is typically supplied by combusting fossil fuels. Our research introduces metamaterial reactors as a new electrified heating platform for decarbonizing thermochemical processes. With proper co-design of the reactor metamaterial baffle with power electronics, volumetric heating is achieved with near-unity conversion of electricity to internal heat.

Reactor scaling to industrially relevant sizes can be readily achieved by customization of the metamaterial baffle. As reactor size increases, the total system efficiency naturally increases and approaches the efficiency of the power electronics (>90%). Our reactor additionally features enhanced heat transfer properties that can enable operation under process-intensified conditions, yielding significant opportunities to reduce reactor size and capital costs in scaled systems.

conductive wall heating, heat exchangers, and convective internal heating.[9] To date, a wide range of electrified heating modalities, including resistive, inductive, microwave, acoustic, and photothermal processes, have been investigated.

Among these options, concepts based on magnetic induction have great potential to scale, and they additionally exhibit several features that are particularly beneficial to thermochemical reactor systems operation. Magnetic fields generated from magnetic induction are intrinsically volumetric, and energy transfer in meter-scale metallurgical induction systems has been demonstrated at megawatt power levels.[10] In addition, induction coils naturally serve as transformers that transduce low input currents to high induced currents, enabling efficient power electronics operating with relatively high voltages and low currents. Furthermore, the wireless nature of power transfer with induction and the elimination of electrical contacts to the heating medium presents immense simplifications in implementation, reduced parasitic heat loss through the contacts themselves,[11] and safer reactor operating conditions.

There are two primary mechanisms of heating through magnetic induction. The first is eddy current heating, where AC magnetic fields couple to and induce eddy currents in an electrical conductor that dissipate as heat.[10] These concepts have been widely deployed in metallurgical heat treatment and melting systems, and they typically involve direct heating of a metal surface or crucible followed by conductive heat transfer. These ideas take the form of wall heating concepts, and in scaled volumetric reactor systems, they yield parasitic radial temperature gradients and limited heat transfer rates. The second is hysteresis heating in which magnetic domains within highly coercive magnetic materials flip in the presence of an AC magnetic field, dissipating heat in the process.[12–14] Significant research efforts have been made to adapt these concepts to thermochemical reactors, particularly with superparamagnetic nanoparticle susceptors,[15] which have been utilized as heat sources in flow reactors for organic synthesis[16] and high-temperature gas reformers.[17,18] However, these magnetic materials have limited stability at high temperatures,[19] cannot be inductively heated beyond their Curie temperatures, and suffer from low coupling efficiencies.[20] Thus, there remain opportunities to deploy inductive heating concepts to thermochemical reactors that are energetically efficient, volumetric, and stable at high temperatures.

In this article, we introduce metamaterial reactors as an innovative concept in electrified chemical reaction engineering that features the volumetric heating of three-dimensional metamaterial reactor baffles. Metamaterials are artificially structured materials with effective physical responses that derive from their detailed geometry and material composition.[21,22] We implement the metamaterial construct within inductively heated reactor systems to enable operating regimes that include efficient volumetric heating and high-temperature stability. In particular, we specify the reactor baffle, here an open-cell ceramic lattice, as a metamaterial susceptor that can be modeled as a homogeneous medium with effective electrical and thermal conductivities. This abstraction enables a reactor-scale description of the induction heating process and the multi-scalar modeling and optimization of its heating and heat transfer properties. We demonstrate volumetric internal reactor heating with near-unity efficiencies and configure our metamaterial reactor to perform the endothermic reverse water-gas shift (RWGS) reaction (i.e., $H_2 + CO_2 \rightarrow H_2O + CO$). The RWGS reaction is particularly promising for electrification and CO_2 utilization, as it converts CO_2 into valuable syngas, which can be further processed into renewable fuels and chemicals such as methanol and other hydrocarbons via

[1]Department of Electrical Engineering, Stanford University, Stanford, CA 94305, USA

[2]Department of Materials Science and Engineering, Stanford University, Stanford, CA 94305, USA

[3]Department of Mechanical Engineering, Stanford University, Stanford, CA 94305, USA

[4]Department of Chemistry, Stanford University, Stanford, CA 94305, USA

[5]These authors contributed equally

[6]Lead contact

*Correspondence: jonfan@stanford.edu

https://doi.org/10.1016/j.joule.2024.07.017

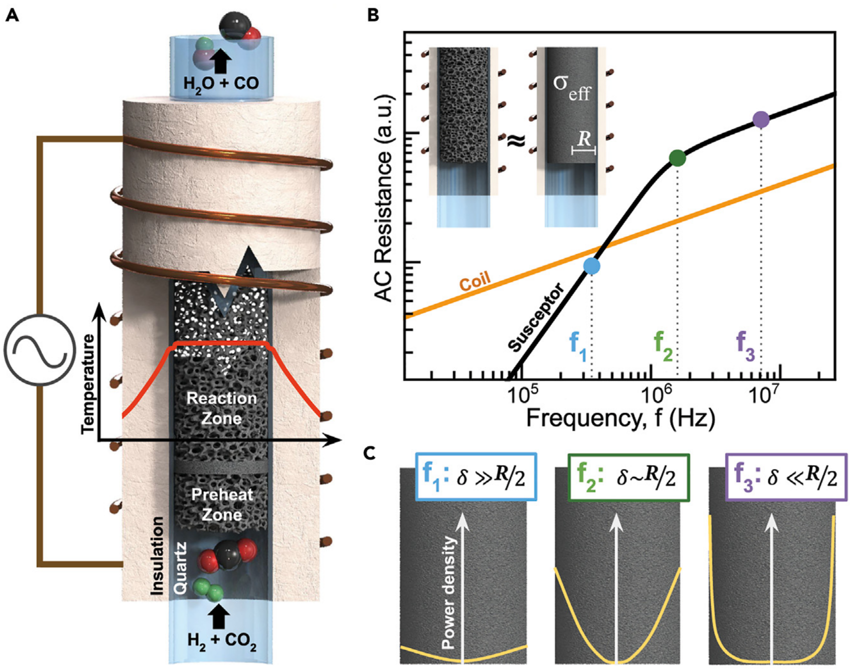

Figure 1. Metamaterial reactor concept

(A) Schematic of our metamaterial reactor configured for the RWGS reaction. A reaction-bonded silicon carbide foam baffle serves as a support for catalyst pellet loading and as a volumetrically heated susceptor with high surface area. The temperature plot shows the cross-sectional temperature profile within the reaction zone of the reactor.

(B) Plot of susceptor and induction coil AC resistance as a function of frequency. The susceptor is modeled as a homogeneous cylinder with a constant effective electrical conductivity.

(C) Power dissipation profiles within the susceptor at different induction frequencies. The ideal operating regime is at f_2, where skin depth ($\delta = \sqrt{1/(\pi\sigma_{eff} f \mu_0)}$) is equal to half of the radius of the reactor (R). This regime features volumetric heating and high dissipated power.

Fischer-Tropsch synthesis.[23–25] As the RWGS process is an endothermic reaction operating at high temperatures, it can significantly benefit from direct, efficient, and fast heat transfer enabled by our inductively heated reactor concept.

RESULTS

Our fixed-bed tubular reactor implementation with the metamaterial susceptor and a helical induction coil is presented in Figure 1A. The cylindrical lab-scale reactor (radius $R = 19$ mm) comprises a quartz tube to ensure that the generated AC magnetic fields couple to the susceptor without parasitic coupling to the reactor walls, as would occur with conventional reactors. The baffle simultaneously serves as a support structure for fixed-bed catalysts and as a high-surface-area heating element that supports enhanced volumetric heat transfer. The fixed-bed catalyst particles consist of ∼1 mm-diameter spherical pellets that readily load into the susceptor. To perform RWGS, we utilize a recently developed class of catalyst based on amorphous potassium carbonate supported on mesoporous alumina.[23] These catalysts possess multiple unique features compared with conventional RWGS catalysts, including suppression of competing Sabatier methanation reactions, resilience to the presence of ppm-level sulfur species in the reactant stream, and low cost. Details pertaining to catalyst preparation and experimental characterization are in the supplemental experimental procedures section “supplementary information on RWGS reactions.”

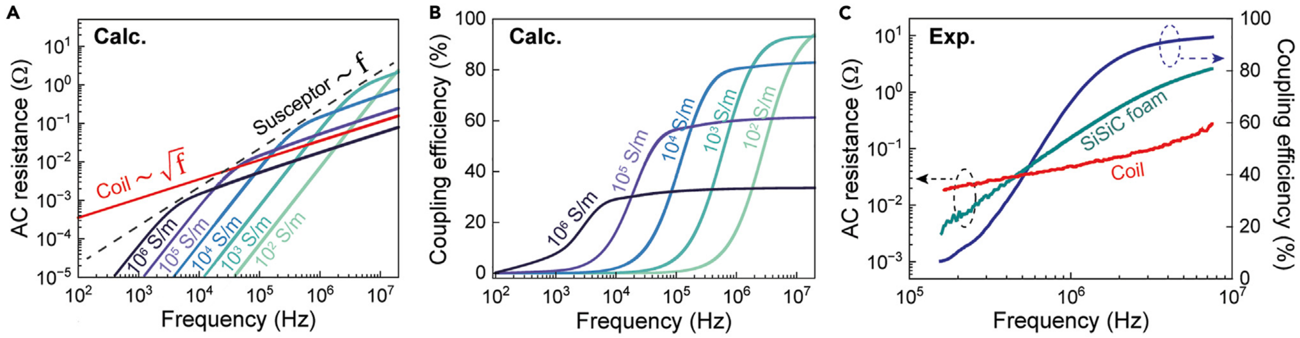

Figure 2. Tailoring of coupling efficiency within the metamaterial reactor

(A) Plot of calculated frequency-dependent AC resistance and scaling trends for a fixed helical copper coil and homogeneous cylindrical susceptors with R = 19 mm and differing electrical conductivity values.

(B) Plot of calculated coupling efficiency as a function of frequency for differing susceptor conductivity values. The coupling efficiency approaches unity at megahertz frequencies for susceptors featuring low conductivities.

(C) Experimental AC resistances and coupling efficiency for our SiSiC cylindrical foam susceptor system. More details on impedance measurements and power electronics setup can be found in supplemental experimental procedures sections "analytic derivation of impedance terms," "experimental susceptor impedance measurements," and "high-frequency power electronics."

Proper co-design of the metamaterial and induction frequency is essential to maximizing susceptor heating efficiency, minimizing parasitic joule heating in the magnetic coil, and enabling volumetric reactor heating. To identify distinct operating regimes in our reactor system, we first consider a general induction heating process involving a homogenous cylindrical susceptor (electrical conductivity σ_{eff}) and helical copper coil. A plot of the real parts of coil and susceptor impedances (Figure 1B), which correspond to the power dissipated in the coil and susceptor, respectively,[26] indicates that amplifier frequency (f) and skin depth ($\delta = \sqrt{1/(\pi\sigma_{\text{eff}} f \mu_0})$ are critical parameters that delineate different regimes for induction heating. At low frequencies, the susceptor heating profile (Figure 1C) is volumetric and its resistance scales as f^2. At frequencies where $\delta \sim R/2$, the scaling of susceptor resistance rolls over to $\sqrt{f}$, and further increases in frequency are accompanied by increasingly concentrated heating profiles at the cylinder walls. The rollover condition at $\delta \sim R/2$ represents an ideal operating regime in which the heating profile is volumetric and power dissipation in the susceptor is maximized.

A more comprehensive impedance analysis is presented in Figure 2A for coil and susceptor dimensions matching our reactor setup and for several values of susceptor σ_{eff}. Coupling efficiency, defined as the ratio of susceptor heating to combined susceptor and coil heating, is readily calculated from these impedances and plotted in Figure 2B. For susceptors featuring relatively high σ_{eff} comparable to standard metal superalloys, it is not possible to achieve high heating efficiency at any frequency. However, as σ_{eff} reduces, the susceptor impedance rollover point shifts to higher frequencies and values, leading to corresponding increases in heating efficiency. Following these trends, we find for our reactor configuration that for susceptors with σ_{eff} below $\sim 10^3$ S/m, the heating efficiency is greater than 90% at megahertz frequencies. With this insight, we set f to 6.78 MHz, which is within a standard industrial, scientific, and medical frequency band.

To achieve the desired metamaterial σ_{eff} and ensure that the metamaterial simultaneously functions as an effective catalyst support and heat transfer medium, we carefully specify both its intrinsic material electrical conductivity (σ_0) and geometric structure. Low intrinsic electrical conductivities are obtained by utilizing

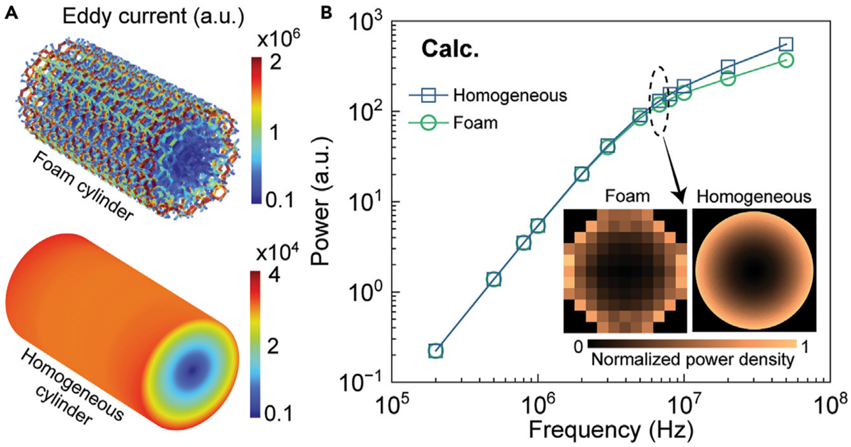

Figure 3. Heating analysis of metamaterial baffle

(A) Simulated eddy current distributions for a foam and a homogeneous cylinder with an σ_{eff} corresponding to the foam.

(B) Plot of total power dissipation as a function of frequency for the foam and homogeneous cylinders. The inset includes cross-sectional heat dissipation profiles in both cylinders at 6.78 MHz. The power density plot of the foam shows volumetrically averaged voxels, each spanning 4 × 4 mm^2 square cross-sectional areas and the length of the cylinder.

electrically conductive ceramics made from reaction-bonded silicon carbide (SiSiC), which also showcases high thermal conductivity, high mechanical strength, and chemical inertness.[27] The structuring of the ceramic metamaterial as an open-cell lattice with high porosity (ε) leads to further reductions in σ_{eff} and ensures that the baffle can be loaded with catalysts, supports the internal flow of gases, and takes up little volume in the reactor. For a highly porous isotropic metamaterial in the low-frequency limit, where mutual inductance effects are negligible,[28] σ_{eff} follows the Lemlich limit[29] and is approximately $\sigma_0(1 - \varepsilon)/\tau$, where τ is the foam tortuosity.

The basic dependence of σ_{eff} on porosity means that there is a wide range of microscopic layouts that satisfy our design criteria for metamaterial induction heating. Down selection of the microscopic metamaterial geometry is determined by reaction engineering considerations, including heat transfer, mass transfer, pressure drop, and fluidic mixing characteristics.[30] In this study, we consider porous SiSiC foam susceptors, which have been previously studied as model reactor baffles for resistive heating due to their excellent heat transfer and electrical conductivity characteristics.[31] We utilize foams comprising ten pores per square inch, which have sufficiently large pore openings to host our fixed-bed catalyst particles and high surface areas (~10 in^2/in^3) to facilitate conductive heat transfer from the susceptor to catalyst particles with high heat transfer rates.[32] Experimental impedance characterization of the foam susceptor (σ_{eff} = 800 S/m) and magnetic coil (Figure 2C) match well with theory and indicates the susceptor can be inductively heated with a coupling efficiency of 93% at 6.78 MHz.

Multi-physics induction heating and heat transfer simulations of the metamaterial, together with that of a homogenous cylinder with an equivalent σ_{eff}, further validate our effective medium approach to susceptor design (Figure 3A). Cross-sectional plots of simulated power dissipation in the foam and homogeneous cylinder (inset of Figure 3B) have good agreement and show volumetric heating profiles that span the full susceptor cross section. The heat dissipation profile for the foam is

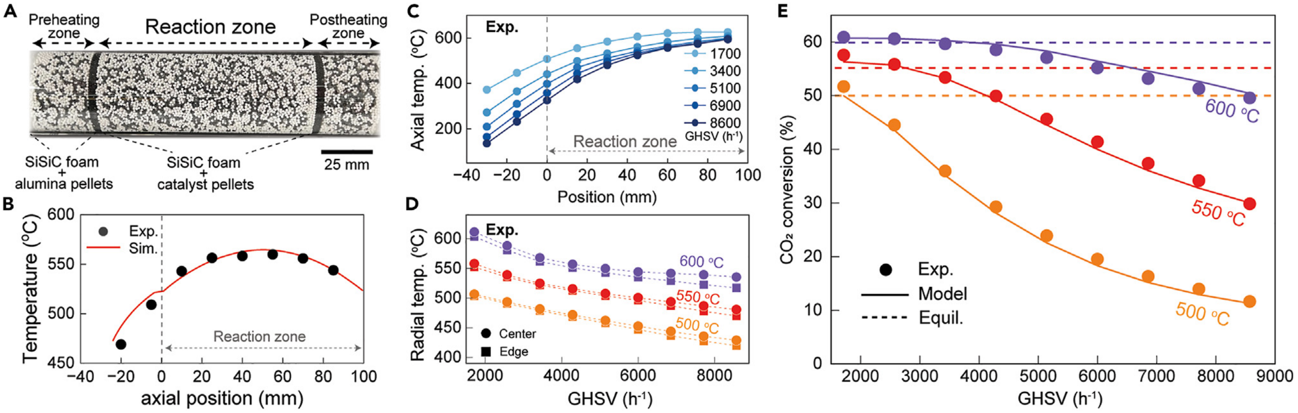

Figure 4. Experimental reactor performance

(A) Photo of the metamaterial reactor configuration with preheating, reaction, and post-heating zones.

(B) Experimental and simulated axial temperature profile within the inductively heated reactor with no gas flow and the exit temperature set to 500°C.

(C) Experimental axial temperature profiles within the reactor for the exit temperature set to 600°C and total GHSV spanning 1,700–8,600 h^{-1}.

(D) Plot of temperatures at the center and edge of the reactor in the middle of the reaction zone as functions of exit temperature and total gas flow rate.

(E) Plot of conversion as a function of total gas flow rate for different exit temperatures, together with curves calculated using a basic plug flow model (solid lines) and equilibrium conversions (dashed lines). The edge temperatures in (D) have a 95% confidence interval of [1.2, −1.2]°C and all other temperature data have a 95% confidence interval of [1.2, −8.2]°C. The uncertainty of the CO_2 conversion is ±1.6%. For detailed error analysis, see supplemental experimental procedures section "supplementary information on RWGS reactions."

volumetrically averaged to facilitate a direct comparison with the homogeneous cylinder profile at macroscopic scales. Plots of total power dissipation in the two systems, as a function of frequency (Figure 3B), are nearly identical. Slight deviations in total power dissipation at high frequencies arise when the heating profile (i.e., skin depth) is on the order of the pore size of the foam and its effective medium description no longer holds.

We next experimentally characterize our metamaterial reactor (implementation details are provided in the supplemental experimental procedures section "reactor setup"). An image of the loaded metamaterial baffle is shown in Figure 4A and delineates the central reaction zone, which is loaded with catalyst pellets, and pre- and post-heating zones, which are loaded with non-catalytic alumina pellets. A key component of our reactor setup is a custom switch-mode push-pull Φ_2 power amplifier[33] that utilizes SiC transistors and operates at 6.78 MHz. Our utilization of wide-band-gap electronics follows recent developments in the power electronics community, where wide-band-gap transistors have been demonstrated to minimize switching losses and thus enhance DC-AC conversion efficiency at amplifier frequencies greater than 1 MHz.[34] By utilizing SiC transistors, we can operate at high bus voltages with exceptional thermal performance.[35] Experimental measurements of amplifier efficiency as a function of output power show that the circuit operates with an efficiency of at least 93% for power levels up to one kilowatt (Figure S3C). Together with our experimental coupling efficiency, we measure our total heating efficiency (i.e., DC power conversion to internal reactor heat) to be 86%. Improvements in coil-susceptor coupling and amplifier efficiency can push this efficiency value to over 90%.

Temperature profiling and control within the reactor is achieved using multiple temperature sensors (Figure S7). A thermocouple placed at the reaction zone exit together with feedback control sets the reaction zone exit temperature. Temperature line scans of the susceptor along its axial symmetry axis are performed using a mechanically translating fiber optic temperature sensor. An additional fiber probe is affixed at the quartz tube-thermal insulation interface in the middle of the reaction zone, and the two fiber sensors together characterize radial temperature uniformity within the reaction zone. Experimental temperature profiling under static gas flow conditions is used to construct a numerical reactor model that accurately captures the heating and heat transfer processes within the reactor (Figure 4B). Experimental thermal analysis of the reactor is also performed using infrared imaging to corroborate our numerical model (see more details in the supplemental experimental procedures sections "simulation and validation of power dissipation profiles in the metamaterial reactor," "volumetric reactor temperature profile characterization without gas flow," and "experimental characterization of radial temperature uniformity with gas flow and reactions").

We characterize RWGS reactor performance by running the reaction at ambient pressures across a range of temperatures and reactant flow rates. The reaction zone exit temperatures are fixed to values between 500°C and 600°C. The reactant gases comprise a 3:1:1 molar ratio of H_2:CO_2:Ar and are flowed at gas hourly space velocities (GHSVs) ranging from 1,700 to 8,600 h^{-1}. Plots of axial temperature profiles as a function of gas flow rate are presented in Figures 4C and S12 and show that the exit temperatures are properly set by temperature feedback. Axial temperature gradients within the reaction zone become increasingly steep as the flow rate and exit temperature each increase due to enhanced convective heat transfer and enhanced energy consumption by the heat of the reaction and gas heating in these reactor operating regimes. The experimental radial temperature gradient at the middle of the reaction zone (Figure 4D) indicates that the radial temperature profile is nearly uniform in this reaction zone section for all flow rates and exit temperatures. Such temperature uniformity is due to the combination of our volumetric internal heating scheme and the high effective thermal conductivity of the metamaterial baffle. These measured radial temperature profiles are consistent with numerical modeling (Figure S9), which further indicates that the radial temperature profiles are effectively uniform throughout the reaction zone.

Plots of CO_2 conversion as a function of gas flow rate for different exit temperatures are shown in Figure 4E. At low gas flow rates, the reactor residence times are relatively long and CO_2 conversion approaches equilibrium values, which increase with increasing exit temperature. As the gas flow rate increases, the reactor residence times reduce and conversion subsequently decreases. For the lowest flow rates, the temperature at the center of the reactor is higher compared with its exit temperature due to position-dependent conductive heat loss within the reactor, resulting in conversions that exceed equilibrium values specified by the exit temperature reference. These effects are properly captured in our thermal and plug flow models in the supplemental experimental procedures sections "volumetric reactor temperature profile characterization without gas flow" and "1D plug flow model of reaction conversion with axial temperature variations," respectively. Good agreement between the plug flow model and experimental data is attributed to the ideal gas mixing and distribution properties of our packed-bed system and the radially uniform temperature distributions in the reaction zone. A continuous 80-h reaction run and repeated reaction cycles between high and low temperatures are also presented in the supplemental experimental procedures section "supplementary information on RWGS reactions." These results indicate that the reactor and catalyst are highly stable during long-duration reaction runs and heating and cooling ramping.

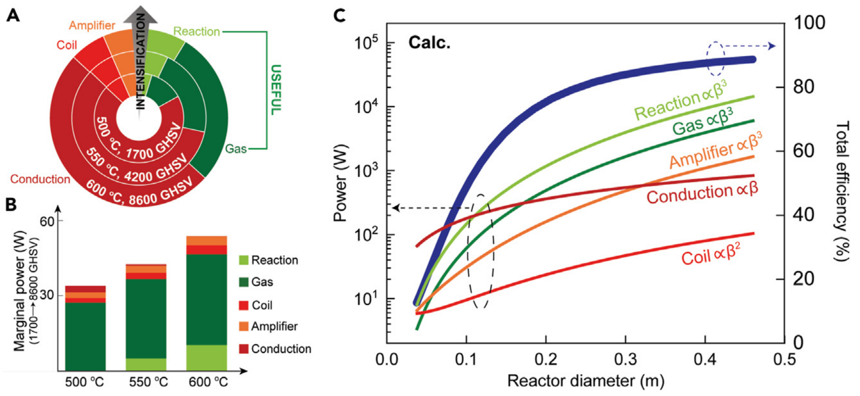

Figure 5. Reactor intensification and scale-up analysis

(A) Chart of experimental reactor energy utilization for increasingly intensified conditions, specified as increases in exit temperature and gas flow rate for a fixed conversion value of 50%.

(B) Experimental marginal power consumption for different exit temperatures, for increases in GHSV from 1,700 to 8,600 h^{-1}.

(C) Theoretical energy utilization and total power efficiency as a function of reactor diameter, together with scaling trends for each energy utilization pathway. β represents a linear scaling factor for the reactor diameter and length.

An analysis of experimental conversion and energy utilization indicates that the total energy efficiency of our reactor increases as the reaction process is intensified. We define total energy efficiency as the energy used for gas heating and the heat of reaction (i.e., useful energy) divided by energy consumed by all energy utilization pathways. We perform this analysis in two ways. First, we plot fractional energy consumption of all energy utilization pathways for combinations of gas flow rates and exit temperatures that correspond to a fixed conversion value of 50%. The results are shown in Figure 5A and indicate that the fraction of energy consumed as useful energy increases from 12.2% to 36.7% as the exit temperature and gas flow rate increase from 500°C and 1,700 h^{-1} to 600°C and 8,600 h^{-1}, respectively. Second, we plot marginal power consumption, which corresponds to the utilization of energy added to the system as the GHSV increases from 1,700 to 8,600 h^{-1}, for different fixed exit temperature values. The plot (Figure 5B) indicates that as gas flow rate increases, ~85% of additional energy added to the system is consumed as useful energy. We anticipate that further improvements to total energy efficiency can be achieved with further intensification of process conditions (i.e., even higher flow rates and reactor pressures), use of better insulation materials, and optimization of the coil geometry.

Finally, we demonstrate the basis for metamaterial reactor scale up and show through scaling trends that the total energy efficiency approaches near-unity values as the reactor size increases. We consider scaling of the reactor diameter and length by the factor β, and we fix the operating frequency to be 6.78 MHz and adjust σ_{eff} so that $\delta = R/2$ as the reactor diameter increases. Such adjustments to σ_{eff} are readily achieved by modifying the metamaterial geometry and material composition. We observe that in the large reactor limit, the useful energy utilization pathways and power amplifier losses scale as β^3, while thermal conduction losses and power losses in the coil scale as β and β^2, respectively (Figure 5C). As such, the total energy efficiency in large reactors converges to the efficiency of the power amplifier. Details pertaining to this analysis are in the supplemental experimental procedures sections "systems energy balance" and "reactor scale up analysis," and a more in-depth scale-up analysis will be a topic of future work.

DISCUSSION

In summary, we present metamaterial reactors as a pioneering paradigm in electrified chemical reaction engineering. With judicious co-design of the metamaterial baffle and power electronics, the reactors can be volumetrically heated with near-unity heating efficiencies, and they can support heat transfer and process-intensification capabilities that are more typical of microreactors. Our proof-of-concept demonstration with the RWGS reaction shows that our reactors can reform green chemical feedstocks with marginal efficiencies of over 85%, indicating that nearly all electrical energy is converted into useful internal heat. Importantly, our concept utilizes fixed-bed catalysts with conventional form factors and features a straightforward pathway to scale. We anticipate that these concepts can apply to a broad range of high-temperature gas reforming reactions and can also be adapted to the high-temperature processing of liquid and solid feedstocks.[36,37] We also anticipate that the excellent heat transfer characteristics and volumetric heating of our baffle makes these concepts ideal in other heating systems, ranging from steam generators and heat transfer fluid boilers[38] to distillation columns[39] and separations systems based on thermal cycling.[40]

Our reaction results and analysis are consistent with a classical understanding of lab-scale fixed-bed flow reactors.[41] It is nonetheless important to verify these reactor properties in the presence of high-frequency magnetic fields and our induction heating mechanism with a metamaterial baffle. We anticipate that the detailed experimental analysis performed here can be adapted to the investigation and characterization of less-ideal inductively heated reactor configurations, such as scaled inductively heated flow reactors. We also acknowledge that our ambient pressure, lab-scale reactor demonstration does not incorporate the multitude of pressurization, heat management, and heat integration strategies that are well known in thermochemical reactor practice.[42] Pressurization schemes for reaction vessels compatible with induction heating have been proposed[43] and can be readily adapted with our reactor concept. An example of a simple heat integration strategy that can be utilized with our reactor system is the use of a countercurrent heat exchanger that can perform heat exchange between the inlet and outlet gas streams, thereby enabling inlet gas preheating.[44] A reactor scaling analysis that accounts for inlet gas preheating is presented in the supplemental experimental procedures section "reactor scale up analysis" and yields qualitatively similar conclusions to those in Figure 5C, which is that the efficiency of the power electronics dictates overall energy efficiency in large-scale reactors.

There exist multiple avenues for future research, many of which arise from the manifold possibilities in metamaterials design, materials selection, and manufacturing pathways. We envision significant opportunities to design metamaterials that support spatially varying, effective electrical conductivity profiles, which can produce arbitrary volumetric heating profiles that enable reactor operation under further idealized reaction engineering conditions. Enhancements in microscopic metamaterial functionality can be enabled by advanced computational design paradigms, such as freeform topology optimization.[45] The experimental implementation of such metamaterial reactors will be augmented by continued advances in ceramics additive manufacturing,[46] which can enable the high-throughput production of metamaterials tailored to specific catalysts and reactions. We also foresee that, with implementation of our power amplifiers operating at megahertz frequencies, temporal volumetric heating control with microsecond resolution can be supported and can drive thermochemical conversion utilizing non-equilibrium thermal pathways.[7] Finally, we anticipate that new systems-level considerations in energy integration will require development in streamlining our electrified, internally heated reactors within chemical production processes.

EXPERIMENTAL PROCEDURES

Resource availability

Lead contact

Requests for further information, resources, or materials should be directed to and will be fulfilled by the lead contact, Jonathan A. Fan (jonfan@stanford.edu).

Materials availability

This study did not generate new unique reagents.

Data and code availability

The data that support the findings of this study are included in the published article and its supplemental experimental procedures, or available from the lead contact upon request.

SUPPLEMENTAL INFORMATION

Supplemental information can be found online at https://doi.org/10.1016/j.joule.2024.07.017.

ACKNOWLEDGMENTS

J.A.F. and M.W.K. acknowledge the Stanford School of Sustainability Accelerator under grant numbers 266899 and 266972. J.A.F. acknowledges the Packard Fellowship Foundation under grant number 2016-65132. We acknowledge fabrication work done at Stanford Nano Shared Facilities supported by the National Science Foundation (NSF) under grant number ECCS-2026822. C.H.L. acknowledges a Gates Millennium Scholarship. C.C. and A.B.H. acknowledge a Stanford Graduate fellowship. D.L.M. acknowledges NSF fellowship.

AUTHOR CONTRIBUTIONS

J.A.F. conceptualized this work. C.H.L., C.W., Z.R., C.C., P.M., D.L.M., and A.B.H. designed and set up the reactor system. C.W., Z.R., C.C., and P.M. performed reactions and numerical modeling. C.H.L. and C.C. designed and configured power electronics. K.T. prepared catalyst. All the work was performed under the supervision of J.A.F., J.R.-D., and M.W.K. All authors contributed to writing this paper.

DECLARATION OF INTERESTS

We have a patent related to this work titled ''Inductive heating with metamaterial susceptors for chemical reactor systems'' pub. no. WO 2023/172776 A2.

Received: April 17, 2024
Revised: June 6, 2024
Accepted: July 23, 2024
Published: August 19, 2024

REFERENCES

1. Thiel, G.P., and Stark, A.K. (2021). To decarbonize industry, we must decarbonize heat. Joule *5*, 531–550. https://doi.org/10.1016/j.joule.2020.12.007.
2. Bollini, P., Diwan, M., Gautam, P., Hartman, R.L., Hickman, D.A., Johnson, M., Kawase, M., Neurock, M., Patience, G.S., Stottlemyer, A., et al. (2023). Vision 2050: reaction engineering roadmap. ACS Eng. Au *3*, 364–390. https://doi.org/10.1021/acsengineeringau.3c00023.
3. Daiyan, R., MacGill, I., and Amal, R. (2020). Opportunities and challenges for renewable power-to-X. ACS Energy Lett. *5*, 3843–3847. https://doi.org/10.1021/acsenergylett.0c02249.
4. Seh, Z.W., Kibsgaard, J., Dickens, C.F., Chorkendorff, I., Nørskov, J.K., and Jaramillo, T.F. (2017). Combining theory and experiment

in electrocatalysis: insights into materials design. Science *355*, eaad4998. https://doi.org/10.1126/science.aad4998.

5. Fan, L., Xia, C., Yang, F., Wang, J., Wang, H., and Lu, Y. (2020). Strategies in catalysts and electrolyzer design for electrochemical CO2 reduction toward C2+ products. Sci. Adv. *6*, eaay3111. https://doi.org/10.1126/sciadv.aay3111.
6. Zhou, L., Swearer, D.F., Zhang, C., Robatjazi, H., Zhao, H., Henderson, L., Dong, L., Christopher, P., Carter, E.A., Nordlander, P., et al. (2018). Quantifying hot carrier and thermal contributions in plasmonic photocatalysis. Science *362*, 69–72. https://doi.org/10.1126/science.aat6967.
7. Dong, Q., Yao, Y., Cheng, S., Alexopoulos, K., Gao, J., Srinivas, S., Wang, Y., Pei, Y., Zheng, C., Brozena, A.H., et al. (2022). Programmable heating and quenching for efficient thermochemical synthesis. Nature *605*, 470–476. https://doi.org/10.1038/s41586-022-04568-6.
8. Mallapragada, D.S., Dvorkin, Y., Modestino, M.A., Esposito, D.V., Smith, W.A., Hodge, B.-M., Harold, M.P., Donnelly, V.M., Nuz, A., Bloomquist, C., et al. (2023). Decarbonization of the chemical industry through electrification: barriers and opportunities. Joule *7*, 23–41. https://doi.org/10.1016/j.joule.2022.12.008.
9. Wismann, S.T., Engbæk, J.S., Vendelbo, S.B., Bendixen, F.B., Eriksen, W.L., Aasberg-Petersen, K., Frandsen, C., Chorkendorff, I., and Mortensen, P.M. (2019). Electrified methane reforming: A compact approach to greener industrial hydrogen production. Science *364*, 756–759. https://doi.org/10.1126/science.aaw8775.
10. Rudnev, V., Loveless, D., and Cook, R.L. (2017). Handbook of Induction Heating, Second Edition (CRC Press). https://doi.org/10.1201/9781315117485.
11. Lucía, O., Maussion, P., Dede, E.J., and Burdío, J.M. (2014). Induction heating technology and its applications: past developments, current technology, and future challenges. IEEE Trans. Ind. Electron. *61*, 2509–2520. https://doi.org/10.1109/TIE.2013.2281162.
12. Dutz, S., Hergt, R., Mürbe, J., Müller, R., Zeisberger, M., Andrä, W., Töpfer, J., and Bellemann, M.E. (2007). Hysteresis losses of magnetic nanoparticle powders in the single domain size range. J. Magn. Magn. Mater. *308*, 305–312. https://doi.org/10.1016/j.jmmm.2006.06.005.
13. Ceylan, S., Coutable, L., Wegner, J., and Kirschning, A. (2011). Inductive heating with magnetic materials inside flow reactors. Chemistry *17*, 1884–1893. https://doi.org/10.1002/chem.201002291.
14. Wang, W., Tuci, G., Duong-Viet, C., Liu, Y., Rossin, A., Luconi, L., Nhut, J.-M., Nguyen-Dinh, L., Pham-Huu, C., and Giambastiani, G. (2019). Induction heating: an enabling technology for the heat management in catalytic processes. ACS Catal. *9*, 7921–7935. https://doi.org/10.1021/acscatal.9b02471.
15. Yassine, S.R., Fatfat, Z., Darwish, G.H., and Karam, P. (2020). Localized catalysis driven by the induction heating of magnetic nanoparticles. Catal. Sci. Technol. *10*, 3890–3896. https://doi.org/10.1039/D0CY00439A.
16. Roman, C.L., da Silva Moura, N., Wicker, S., Dooley, K.M., and Dorman, J.A. (2022). Induction heating of magnetically susceptible nanoparticles for enhanced hydrogenation of oleic acid. ACS Appl. Nano Mater. *5*, 3676–3685. https://doi.org/10.1021/acsanm.1c04351.
17. Mortensen, P.M., Engbæk, J.S., Vendelbo, S.B., Hansen, M.F., and Østberg, M. (2017). Direct hysteresis heating of catalytically active Ni–Co nanoparticles as steam reforming catalyst. Ind. Eng. Chem. Res. *56*, 14006–14013. https://doi.org/10.1021/acs.iecr.7b02331.
18. Vinum, M.G., Almind, M.R., Engbaek, J.S., Vendelbo, S.B., Hansen, M.F., Frandsen, C., Bendix, J., and Mortensen, P.M. (2018). Dual-function cobalt–nickel nanoparticles tailored for high-temperature induction-heated steam methane reforming. Angew. Chem. Int. Ed. Engl. *57*, 10569–10573. https://doi.org/10.1002/anie.201804832.
19. Hou, L., Zhen, X., Liu, L., Kuang, D., Gao, Y., Luo, H., Deng, L., Chen, C., and Wang, S. (2021). Synthesis, thermal stability, magnetic properties, and microwave absorption applications of CoNi-C core-shell nanoparticles with tunable Co/Ni molar ratio. Results Phys. *22*, 103893. https://doi.org/10.1016/j.rinp.2021.103893.
20. Di Corato, R., Espinosa, A., Lartigue, L., Tharaud, M., Chat, S., Pellegrino, T., Ménager, C., Gazeau, F., and Wilhelm, C. (2014). Magnetic hyperthermia efficiency in the cellular environment for different nanoparticle designs. Biomaterials *35*, 6400–6411. https://doi.org/10.1016/j.biomaterials.2014.04.036.
21. Kadic, M., Bückmann, T., Schittny, R., and Wegener, M. (2013). Metamaterials beyond electromagnetism. Rep. Prog. Phys. *76*, 126501. https://doi.org/10.1088/0034-4885/76/12/126501.
22. Liu, Y., and Zhang, X. (2011). Metamaterials: a new frontier of science and technology. Chem. Soc. Rev. *40*, 2494–2507. https://doi.org/10.1039/C0CS00184H.
23. Li, C.S., Frankhouser, A.D., and Kanan, M.W. (2022). Carbonate-catalyzed reverse water-gas shift to produce gas fermentation feedstocks for renewable liquid fuel synthesis. Physiol. Sci. *3*, 101021. https://doi.org/10.1016/j.xcrp.2022.101021.
24. Schmidt, P., Batteiger, V., Roth, A., Weindorf, W., and Raksha, T. (2018). Power-to-liquids as renewable fuel option for aviation: a review. Chem. Ing. Tech. *90*, 127–140. https://doi.org/10.1002/cite.201700129.
25. Joo, O.-S., Jung, K.-D., Moon, I., Rozovskii, A.Ya., Lin, G.I., Han, S.-H., and Uhm, S.-J. (1999). Carbon Dioxide Hydrogenation to Form methanol via a Reverse-Water-Gas-Shift Reaction (the CAMERE Process). Ind. Eng. Chem. Res. *38*, 1808–1812. https://doi.org/10.1021/ie9806848.
26. Nagel, J.R. (2018). Induced eddy currents in simple conductive geometries: mathematical formalism describes the excitation of electrical eddy currents in a time-varying magnetic field. IEEE Antennas Propag. Mag. *60*, 81–88. https://doi.org/10.1109/MAP.2017.2774206.
27. Sangsuwan, P., Orejas, J.A., Gatica, J.E., Tewari, S.N., and Singh, M. (2001). Reaction-bonded silicon carbide by reactive infiltration. Ind. Eng. Chem. Res. *40*, 5191–5198. https://doi.org/10.1021/ie001029e.
28. Pendry, J.B., Holden, A.J., Stewart, W.J., and Youngs, I. (1996). Extremely low frequency plasmons in metallic Mesostructures. Phys. Rev. Lett. *76*, 4773–4776. https://doi.org/10.1103/PhysRevLett.76.4773.
29. Lemlich, R. (1978). A theory for the limiting conductivity of polyhedral foam at low density. J. Colloid Interface Sci. *64*, 107–110. https://doi.org/10.1016/0021-9797(78)90339-9.
30. Kapteijn, F., and Moulijn, J.A. (2022). Structured catalysts and reactors – perspectives for demanding applications. Catal. Today *383*, 5–14. https://doi.org/10.1016/j.cattod.2020.09.026.
31. Zheng, L., Ambrosetti, M., Marangoni, D., Beretta, A., Groppi, G., and Tronconi, E. (2023). Electrified methane steam reforming on a washcoated SiSiC foam for low-carbon hydrogen production. AIChE J. *69*, e17620. https://doi.org/10.1002/aic.17620.
32. Visconti, C.G., Groppi, G., and Tronconi, E. (2016). Highly conductive “packed foams”: A new concept for the intensification of strongly endo- and exo-thermic catalytic processes in compact tubular reactors. Catal. Today *273*, 178–186. https://doi.org/10.1016/j.cattod.2016.02.060.
33. Gu, L., Zulauf, G., Zhang, Z., Chakraborty, S., and Rivas-Davila, J. (2020). Push–pull class \Phi _\text2 RF power amplifier. IEEE Trans. Power Electron. *35*, 10515–10531. https://doi.org/10.1109/TPEL.2020.2981312.
34. Zulauf, G., Tong, Z., Plummer, J.D., and Rivas-Davila, J.M. (2019). Active power device selection in high- and very-high-frequency power converters. IEEE Trans. Power Electron. *34*, 6818–6833. https://doi.org/10.1109/TPEL.2018.2874420.
35. Millán, J., Godignon, P., Perpiñà, X., Pérez-Tomás, A., and Rebollo, J. (2014). A survey of wide bandgap power semiconductor devices. IEEE Trans. Power Electron. *29*, 2155–2163. https://doi.org/10.1109/TPEL.2013.2268900.
36. Almind, M.R., Vendelbo, S.B., Hansen, M.F., Vinum, M.G., Frandsen, C., Mortensen, P.M., and Engbæk, J.S. (2020). Improving performance of induction-heated steam methane reforming. Catal. Today *342*, 13–20. https://doi.org/10.1016/j.cattod.2019.05.005.
37. Eigenberger, G., and Ruppel, W. (2012). Catalytic fixed-bed reactors. In Ullmann’s Encyclopedia of Industrial Chemistry (John Wiley & Sons, Ltd). https://doi.org/10.1002/14356007.b04_199.pub2.
38. Saidur, R., Ahamed, J.U., and Masjuki, H.H. (2010). Energy, exergy and economic analysis of industrial boilers. Energy Policy *38*,

2188–2197. https://doi.org/10.1016/j.enpol.2009.11.087.

39. Cui, C., Qi, M., Zhang, X., Sun, J., Li, Q., Kiss, A.A., Wong, D.S.-H., Masuku, C.M., and Lee, M. (2024). Electrification of distillation for decarbonization: an overview and perspective. Renew. Sustain. Energy Rev. *199*, 114522. https://doi.org/10.1016/j.rser.2024.114522.

40. Moate, J.R., and LeVan, M.D. (2010). Temperature swing adsorption compression: effects of nonuniform heating on bed efficiency. Appl. Therm. Eng. *30*, 658–663. https://doi.org/10.1016/j.applthermaleng.2009.11.013.

41. Fogler, H.S. (2020). Elements of Chemical Reaction Engineering (Pearson).

42. Linnhoff, B., and Hindmarsh, E. (1983). The pinch design method for heat exchanger networks. Chem. Eng. Sci. *38*, 745–763. https://doi.org/10.1016/0009-2509(83)80185-7.

43. Armstrong, T., Deeg, M., Larimer, J., Larson, W., Mccoy, K., Molnar, M.J., and Schultz, J.A. (2014). Induction Heating Apparatus.

44. Bergman, T.L. (2011). Fundamentals of Heat and Mass Transfer (John Wiley & Sons).

45. Sell, D., Yang, J., Doshay, S., Yang, R., and Fan, J.A. (2017). Large-angle, multifunctional metagratings based on freeform multimode geometries. Nano Lett. *17*, 3752–3757. https://doi.org/10.1021/acs.nanolett.7b01082.

46. Lakhdar, Y., Tuck, C., Binner, J., Terry, A., and Goodridge, R. (2021). Additive manufacturing of advanced ceramic materials. Prog. Mater. Sci. *116*, 100736. https://doi.org/10.1016/j.pmatsci.2020.100736.

Joule, Volume *8*

Supplemental information

Electrified thermochemical reaction systems with high-frequency metamaterial reactors

Calvin H. Lin, Chenghao Wan, Zhennan Ru, Connor Cremers, Pinak Mohapatra, Dolly L. Mantle, Kesha Tamakuwala, Ariana B. Höfelmann, Matthew W. Kanan, Juan Rivas-Davila, and Jonathan A. Fan

Note S1. Reactor setup

Our electrified thermochemical reactor system comprises a fixed bed reactor hosting our metamaterial baffle and catalyst pellets, a power amplifier operating at megahertz frequencies (see Note S4 for more details), a helical copper induction coil, mass flow control infrastructure for gas handling, temperature sensors, software that supports automated reactor controls, and a mass spectrometer. Temperature monitoring and closed loop feedback are achieved using a custom-developed automation system. Details pertaining to temperature measurements are in Notes S6 and S7. Temperature and mass spectrometer measurements are logged using a Python script.

The reactor (Figure S1A) consists of an 800 mm-long quartz tube with an inner diameter of 39 mm. The quartz tube is sealed by two flanges with integrated gas ports and temperature sensor ports, and it is surrounded by 25 mm-thick aluminosilicate thermal insulation (Zircar Ceramics, Inc.). A copper helical induction coil comprising 6.35 mm-diameter copper tubing, 100 mm-diameter helical loops, and 7 turns is placed in a concentric position in the middle of the reactor. Both the induction coil and flanges are mounted on acrylic holders that minimize parasitic magnetic field coupling and heating. Inlet gases are controlled using a set of mass flow controllers (Alicat Scientific) and outlet gases are flowed through a water condenser and analyzed by a commercial mass spectrometer (MKS Cirrus 3) before being directed to an exhaust port.

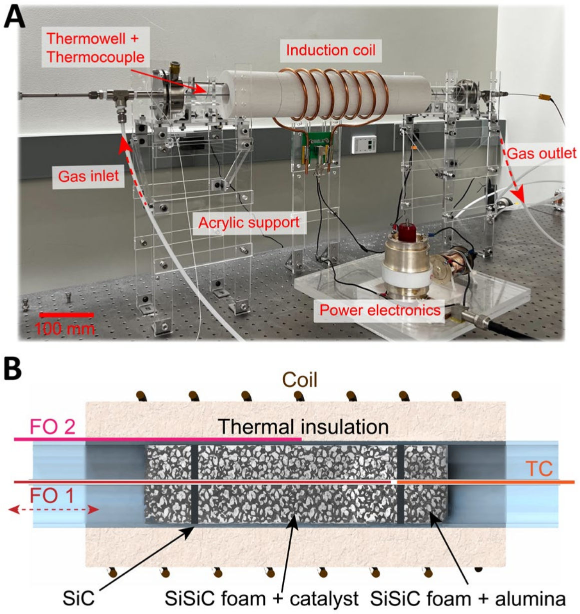

Figure S1. Experimental RWGS reactor system. (**A**) Image of our insulated RWGS reactor mounted using acrylic supports. **(B)**. Schematic of the reaction section inside the quartz reactor. The foam susceptor is packed with catalyst pellets and held in place using quartz wool (not pictured) on either end of the susceptor. The exit temperature is controlled and monitored using a type-K thermocouple (TC). The central axial temperature is measured using a motorized fiber optic sensor (FO 1). A second fiber sensor (FO 2) is placed in a fixed position at the interface between the insulation and quartz tube to measure the radial temperature profile.

The RWGS reaction happens within the central region of the tube, which hosts a 150-mm long metamaterial susceptor that serves as the inductively heated element (Figure S1B). Its central region, serving as the reaction zone, is composed of a 100 mm-long reaction section consisting of 10 Pores Per Inch (PPI) reaction bonded silicon carbide (SiSiC) foam (manufactured by EngiCer SA) packed with spherical catalyst pellets. The catalyst pellets consist of mesoporous gamma phase alumina spherical supports with 18 wt% loading of alkali carbonate (more details in Note S10). This reaction zone foam is sandwiched by 3 mm-thick 100-PPI SiC discs (ERG Aerospace Corp.) on each side, which hold the catalyst pellets in the reaction zone in place, followed by 25-mm long SiSiC foams packed with porous alumina pellets (i.e., unfunctionalized catalyst carrier). The 25 mm-long end sections impregnated with alumina pellets serve two roles: 1) it reduces the presence of axial temperature gradients in the reaction zone that arise from parasitic heat loss at the susceptor-quartz tube interface; and 2) the end piece at the reaction zone inlet serves as a gas distributor and preheater. All SiSiC and SiC sections feature ~4 mm-diameter holes along the axial symmetry axis of the cylinder that supports threading of a thermowell through the reactor tube.

Our power electronics approach in providing power from the wall to the reactor involves AC-DC-AC conversion with a custom-built power amplifier (see Note S4 for detailed implementation). To utilize the thermocouple during magnetic induction heating in a manner that mitigates electromagnetic interference from the induction coil, the DC power supply unit is pulsed on/off with a 90% duty cycle, and thermocouple measurements are performed only when the supply is off. To quickly reach a setpoint temperature at the reactor outlet as measured with the thermocouple, closed loop feedback via a PID controller is implemented that dynamically adjusts the supply voltage of the power supply.

Note S2. Analytic derivation of impedance terms

For our induction frequencies of interest, the pore size of our SiSiC foam is much smaller than the free space wavelength of the electromagnetic field, which is 30 m at 10 MHz and even larger at lower frequencies. In this regime, the foam can be treated as a homogeneous medium with an effective conductivity σ_{eff} that depends on the pore geometry and material composition. We further analyze and justify this effective medium approximation with analytic and numerical analyses in Note S5.

Following this effective medium approximation, we can analytically compute the volumetrically averaged impedance and power dissipation in an inductively heated non-magnetic susceptor. We consider a susceptor with a radius R in the presence of an axially oriented magnetic field with magnitude B_0. We assume the susceptor and coil both have a total length of L and we define the complex wavenumber $\kappa = \sqrt{-i\omega\sigma_{eff}\mu_0}$, where *w* is the angular frequency, $\omega = 2\pi f$, where *f* is the frequency in Hz. Using an analysis discussed in (*S1*, *S2*), the magnetic field profile is described using the Helmholtz equation:

$$r^2\frac{\partial^2 B_e}{\partial r^2} + r\frac{\partial B_e}{\partial r} + \kappa^2 r^2 B_e = -\kappa^2 r^2 B_0 \quad (r \leq R) \quad \text{(S1)}$$

B_e, the induced magnetic fields, are expressed in cylindrical coordinates:

$$B_e = B_e(r)\hat{z};\ \frac{\partial}{\partial\phi} = \frac{\partial}{\partial z} = 0 \qquad \text{(S2)}$$

By solving the Helmholtz equation and employing Ampere's Law, the eddy current density within the susceptor is:

$$\boldsymbol{J}(r) = \frac{\kappa B_0}{\mu_0}\left[\frac{J_1(\kappa r)}{J_0(\kappa R)}\right]\hat{\phi} \quad (r \leq R) \qquad \text{(S3)}$$

where J_i is the Bessel function of the order i. Total power dissipation (P_{diss}) is obtained by integrating the square of the current density over the volume of the cylinder:

$$P_{diss} = \frac{1}{2\sigma_{eff}}\int |\boldsymbol{J}|^2 dV = \frac{2\pi\omega B_0^2 L R^2}{\mu_0} Im\left\{\frac{J_2((1+i)\frac{R}{\delta})}{J_0((1+i)\frac{R}{\delta})}\right\} \qquad \text{(S4)}$$

where δ is the skin depth in the susceptor. In the long solenoid approximation, the magnetic field B_0 in the susceptor, normalized by coil length, is expressed as:

$$B_0 = \mu_0\frac{N}{L}I \qquad \text{(S5)}$$

where N is the number of turns in the coil, and I is the root mean square current in the coil. The impedance of the susceptor, R_{susc}, is:

$$R_{susc} = \frac{2\pi\omega\mu_0 N^2 R^2}{L} Im\left\{\frac{J_2((1+i)\frac{R}{\delta})}{J_0((1+i)\frac{R}{\delta})}\right\} \text{(S6)}$$

For our copper induction coil, we use the improved Dowell's method[S3] that factors in skin and proximity effects to approximate its AC resistance:

$$R_{coil} = \frac{\pi^{3/4} d N^{3/2}}{\sigma_c \delta_c \sqrt{R_c L}} \qquad \text{(S7)}$$

where d is the diameter of the coil, σ_c is the electrical conductivity of copper, R_c is the radius of the copper tube, and δ_c is the skin depth of the copper tube.

The coupling efficiency, at frequencies away from the helical coil resonance, is calculated to be:

$$\eta_{coupling} = \frac{R_{susc}}{R_{susc} + R_{coil}} \quad \text{(S8)}$$

Note S3. Experimental susceptor impedance measurements

To measure susceptor impedance at room temperature, we utilize small-signal impedance measurements of the susceptor placed inside a helical coil using a vector network analyzer (Bode 100). The vector network analyzer measures impedance parameters, and the real part of impedance is AC resistance. To de-embed the resistance of the coil from the resistance of the susceptor, we make two measurements: (1) the impedance of the coil with the susceptor loaded; and (2) the impedance of the coil alone. We then subtract these measurements to obtain the impedance of the susceptor. Proximity effects between the susceptor and coil are neglected, which is justified in the limit where the coil diameter is twice that of the susceptor.

To perform impedance measurements of the susceptor (38 mm diameter SiSiC foam used in the main text) at different temperatures, we place the susceptor inside a thermally insulated quartz tube and flow in hot nitrogen gas, which is heated using a programmable furnace. The susceptor heats through convection, and its temperature is monitored using a thermocouple that is in contact with the susceptor. A water-cooled copper coil surrounding the insulated tube is used for impedance measurements. Water cooling ensures that the coil temperature is fixed to reduce resistive losses. A plot of susceptor impedance as a function of temperature is shown in Figure S2 and indicates that as the temperature changes from room temperature to 540 °C, the impedance experiences minimal variations. Note that, although the temperature dependency is minor, we observed slight changes in the electrical conductivity of the SiSiC foam upon heating, which could affect the coupling efficiency by a few percent. This issue can be addressed by re-tuning our matching network (see the next Note S4 for details) at high temperatures (e.g., ~400 °C).

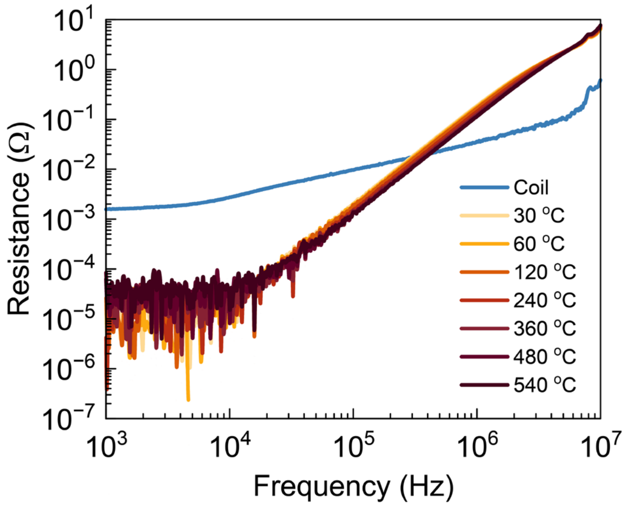

Figure S2. Experimental temperature-dependent AC resistance of the susceptor from 30 to 540 °C.

Note S4. High frequency power electronics

Linear power amplifiers (PA), such as classes A, B, AB, and C PAs, have efficiencies capped below 80% due to transistor conduction losses. On the other hand, switch-mode amplifiers, such as classes E,F, and EF PAs and their variants, minimize overlap between current and voltage at each switching cycle and have theoretical maximum efficiencies of 100%. With our demand of a highly efficient PA, which is a requirement for our application, we design and construct a 6.78 MHz push-pull class Φ_2 amplifier capable of delivering up to 1 kW. The class Φ_2 amplifier features a second harmonic short at the drain that shapes the drain voltage waveform to appear trapezoidal and reduces the peak voltage stress to 2.2 times the DC input voltage. For reference, the transistor in a class E amplifier sees a peak voltage of 3.6 times the DC input voltage. By operating each branch 180° out of phase and combining the outputs at the load, this configuration increases output power without increasing transistor stress, reduces input current ripple, and eliminates even numbered harmonics in a manner that relaxes filtering requirements at the output. We utilize SiC MOSFETs (Wolfspeed C3M0060065L-TR) that have excellent thermal resistance properties and innate protection against avalanche breakdown. We drive the SiC MOSFETs with an auxiliary resonant gate driver that reduces the power consumption by 65% compared to a conventional gate driver.

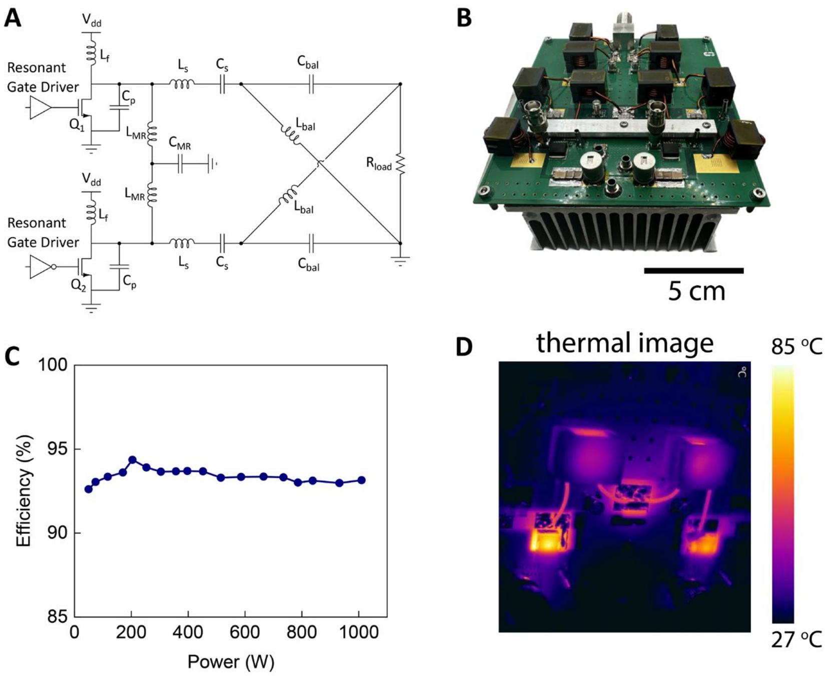

Figure S3. **Power amplifier design and implementation. (A)** Circuit schematic of our push-pull class Φ_2 amplifier. **(B)** Image of the constructed amplifier. **(C)** Experimental drain efficiency across a wide load range. The efficiency is approximately 93% across the load range and reaches a peak of 94% at 200 W. **(D)** Thermal image of the amplifier, taken using an infrared camera (FLIR A655sc), at 1 kW continuous amplifier operation. Each SiC MOSFET reaches a case temperature of approximately 85 °C.

A circuit schematic of our PA is shown in Figure S3A and shows our resonant gate driver, the primary power stage, and lattice balun. The balun serves two functions: (1) to perform impedance matching at a single frequency in a manner that optimally drives the load as seen by the amplifier; and (2) to convert the differential signal to a single-ended signal that drives the ground-referenced load. The balun also allows use of a grounded RF power meter to track the PA output power. The experimentally fabricated circuit is shown in Figure S3B. An experimental measurement of drain efficiency as a function of power output is shown in Figure S3C and indicates that the PA consistently operates with an efficiency of 93% across a wide load range of 50 W to 1 kW. The peak drain efficiency is measured to be 94%. The PA exhibits marginally lower efficiencies at lower powers due to the nonlinear drain capacitance of the transistor at lower input voltages, which prevents the transistors from soft switching. Above 65 V, the drain capacitance (C_{oss}) of the MOSFETs reaches its minimum, allowing the transistors to operate in the zero-voltage switching condition. Power losses are primarily due to heat dissipation in the MOSFETs, as shown in the thermal image of the PA operating at its maximum power of 1 kW (Figure S3D). The thermal image shows that the MOSFETs reach a temperature of about 85 ^{o}C, which is well under the 150 ^{o}C absolute maximum rating of the SiC transistors.

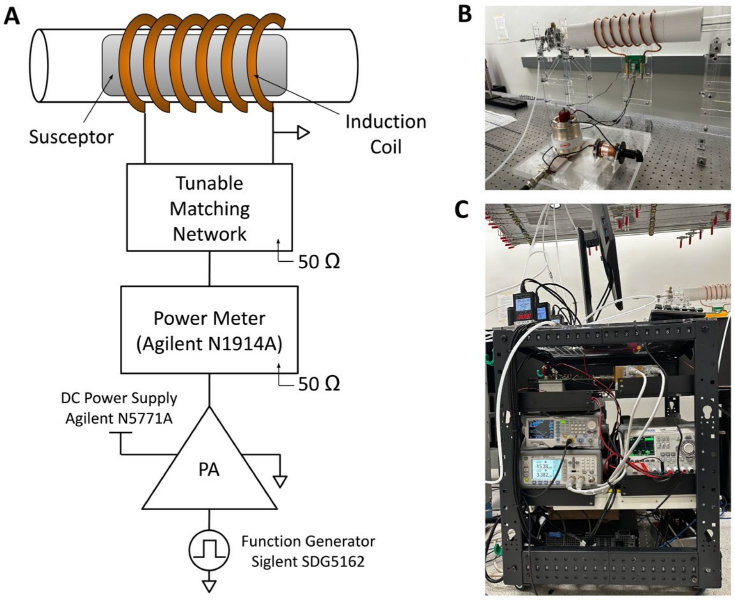

Figure S4. Power electronics driving the reactor. **(A)** Schematic overview of electronic equipment used to power the reactor. **(B)** Image of the tunable matching network with two variable vacuum capacitors. **(C)** Image of the electronics rack that includes DC power supplies, power meter, power amplifier, and computer for controls and operation.

A schematic of our complete power system is shown in Figure S4A. The power amplifier gate drivers utilize two 0-to-5-volt square wave signals, which are 180° out-of-phase at 6.78 MHz, from a function generator (Siglent SDG5162). The signal is then amplified with the 1.5 kW DC power supply (Agilent N5771A). For high power RF measurements, an in-line dual directional coupler (Werlatone C3807) capable of handling AC power sources of up to 5.25 kW, from 300 kHz to 30 MHz, is used. An RF power meter and its sensors interface with the coupler, (Agilent N1914A, N8428A) and measures its forward, reflected, and net power delivery. All of these electronics sit in a custom electronics rack, shown in Fig S4C. The induction coil and susceptor together present mostly an inductive load, and a matching network must be implemented to convert this impedance to a purely resistive load to ensure high power delivery to the susceptor. Additionally, the matching network must make the load appear as 50 Ω because the in-line directional coupler has an output impedance of 50 Ω. We construct a tunable matching network using two variable vacuum capacitors (Jennings GCS-90-15S, 5-90 pF, and Comet CV1C-500NM/10, 80-500 pF) in an L-match configuration, as shown in Figure S4B, which covers a wide impedance range. The power meter allows us to make in situ measurements of the forward and reflected power, which measures the quality of the impedance match. To measure the impedance looking into the matching network, we use the Bode 100 vector network analyzer in a one port reflection configuration and make on-the-fly adjustments to maintain a 50 Ω input impedance and maximize power delivery.

Note S5. Simulation and validation of power dissipation profiles in the metamaterial reactor

The eddy current profiles in our cylindrical reactors can be simulated using the electromagnetic finite element method, which we implement using COMSOL Multiphysics. We utilized the embedded Multiphysics module for induction heating, which couples the magnetic field module (simulating the induced eddy currents) with the heat transfer in solids module (simulating the resulting temperature profile due to the eddy currents). These modules follow the classical Maxwell equations, heat-transfer equations, and Fourier's law of heat conduction, as detailed in the COMSOL handbook[S4].

As an initial step, we build a two-dimensional (2D) model to simulate the inductive heating power profile within a homogeneous cylindrical susceptor with a constant electrical conductivity, and we validate our model by comparing the results with the analytical solution from Note S2. As depicted in Figure S5A, the model features rotational symmetry along the axis at $r = 0$, which enforces cylindrical symmetry. The susceptor and copper induction coils are embedded in a simulation domain comprising air, and infinite element boundaries are used. The susceptor is specified to have a radius of 19 mm and a conductivity of 410 S/m, and the currents in the induction coil have a frequency of 6.78 MHz. The susceptor dimensions, conductivity, and induction frequency are specified such that the skin depth in the cylinder is $R/2$, which is the ideal operational condition discussed in the main text. Note that we applied layer meshing within the susceptor region, with the layer thickness on the order of one-tenth of the skin depth, to ensure the heating profile is well resolved. For the rest of the domains, we used conventional triangular meshing set to the predefined extra fine level. Figure S5B shows the simulated Joule heating power density within the susceptor together with the analytical solution, confirming the accuracy of our numerical model.

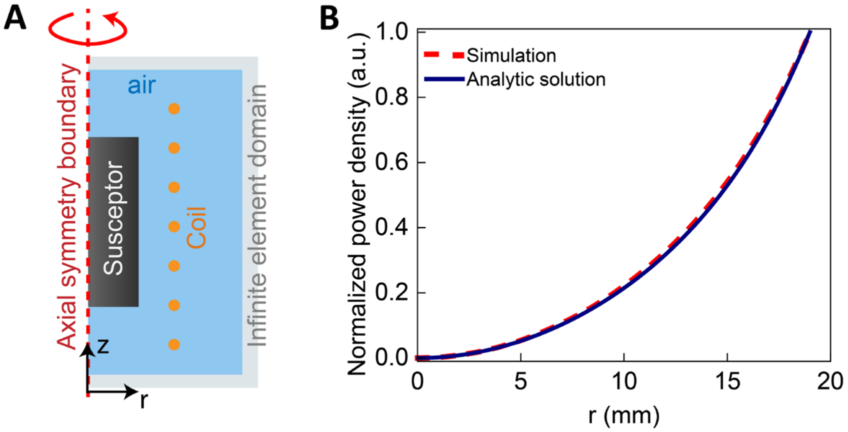

Figure S5. Numerical model of inductively heated susceptor with homogeneous electrical conductivity. (**A**) Schematic of our electromagnetic simulation setup in COMSOL Multiphysics. (**B**) Comparison of normalized power density distribution within the cylindrical susceptor, calculated using analytic and numerical methods.

We follow this analysis by numerically modeling the induction heating of a more realistic 3D susceptor structure and comparing it with an equivalent effective medium model. In this aim, we construct and simulate an open cell foam structure implemented in nTop. The foam comprises Weaire-Phelan structures with 6 mm periodicity, wire thicknesses of 0.55 mm, and strut electrical conductivities of 10000 S/m. The structure type, porosity of 88%, and electrical conductivity were chosen to closely match the experimental random open-cell SiSiC foam. The foam was shaped into a cylindrical susceptor with a diameter of 38 mm and a length of 75 mm (Figure S6A). The length of the foam was chosen to balance simulation time with simulation accuracy.

To construct an effective medium analogue to this 3D open-cell foam susceptor, we calculate the effective electrical conductivity of the 3D foam and utilize this effective conductivity value to model a homogeneous cylindrical susceptor. The effective electrical conductivity of the 3D foam susceptor with porosity ε is calculated using the Lemlich law defined in the main text:

$$\sigma_{eff} = \sigma_0 \times \frac{1-\varepsilon}{\tau} \qquad \text{(S9)}$$

The tortuosity value τ is determined through simulation to be 2.95, which agrees well with previous studies[S5].

The simulated eddy current and power density (for one cross section) of the inductively heated 3D foam susceptor and its homogeneous effective medium analogue are plotted in Figure S6A-B for an induction frequency of 6.78 MHz. For the foam power density plot in Figure S6B, we show the volumetrically averaged power density across axial channels within each 4-by-4-mm square cross section, enabling a clearer and more direct comparison of macroscopic power density distribution with that of the continuous cylinder. A comparison between the two power density profiles reveals good agreement. The integrated powers within the 3D foam and effective medium susceptor are 130.6 W and 121.8 W at 6.78 MHz, respectively, which are comparable. These results indicate the efficacy of our effective medium approach to describe macroscopic induction heating trends (i.e., volumetric profile, total power dissipation, and coupling efficiency) involving our metamaterial susceptor.

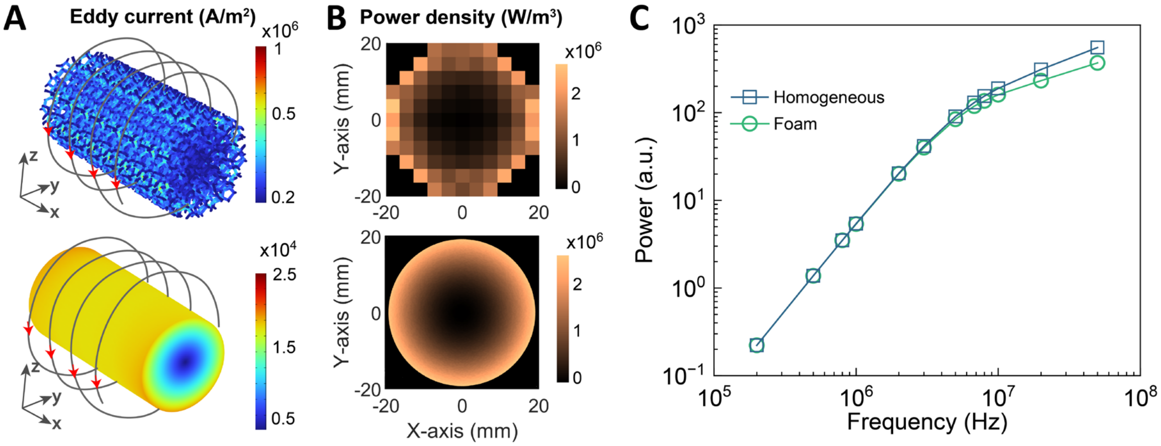

Figure S6. Comparison of power dissipation in an open cell foam susceptor and a homogeneous cylindrical susceptor. (A, B) Simulated induced Eddy current (A) and volumetrically averaged power density (B) in the foam and homogeneous cylindrical susceptor at 6.78 MHz. The homogeneous susceptor electrical conductivity is specified by treating the foam in the effective medium limit, as governed by the Lemlich law. **(C)** Integrated power dissipated in both structures for frequencies ranging from 10^5 to 10^8 Hz, demonstrating good agreement.

We also compare power dissipation trends between the foam and the effective medium cylinder by performing a parametric sweep of the induction frequency from 200 kHz to 10 MHz (Figure S6C). At low frequencies, the differences in power dissipation are negligible. In this regime, the induced magnetic field profile within the susceptor varies with a length scale that is on the order of the susceptor radius. This length scale is much larger than the pore size of the metamaterial susceptor, such that the susceptor can be effectively described in the effective medium regime. At frequencies higher than the inflection point, the magnetic field profile within the susceptor varies with a length scale that is on the order of the skin depth, which decreases as the frequency increases. When the skin depth becomes comparable to the pore size, the lattice can no longer be described in the effective medium limit and the integrated power from the foam susceptor deviates from that of the homogeneous cylindrical susceptor.

In summary, we have demonstrated through numerical experiments that for frequencies at or below the rollover point, the macroscopic power dissipation profile and total power dissipation within the 3D metamaterial susceptor can be effectively captured using a homogeneous susceptor model in the effective medium regime. This simplification will enable reactor modeling with significant computational savings, and it provides a simple interpretable framework for susceptor design and optimization. We will utilize this effective medium description moving forward in our analysis of heating and the combination of heating and heat transfer.

Note S6. Volumetric reactor temperature profile characterization without gas flow

Our approach to quantifying the volumetric temperature profile in the reaction zone without gas flow involves a combination of experimental and numerical analyses. Experimentally, we utilize a combination of thermocouple and fiber optic (FO) temperature probes to quantify the temperature profile along the symmetry axis of the cylindrical susceptor, and at a fixed point of the quartz-insulation interface in the middle of the reaction zone. Numerically, we utilize a steady-state electromagnetics and heat transfer multiphysics finite element model, implemented in COMSOL Multiphysics, to model the temperature profile within the reactor. Realistic thermal conductivity values of reactor components and thermal resistance values at component interfaces are implemented in the model to capture the detailed heat transfer processes in the reactor. Through a parametric analysis, an effective thermal conductivity value describing the heterogeneous susceptor-catalyst pellet materials system is extracted in a manner that is consistent with simulations and experiments. This fitted parameter is then used to characterize the three-dimensional temperature profile within the reactor.

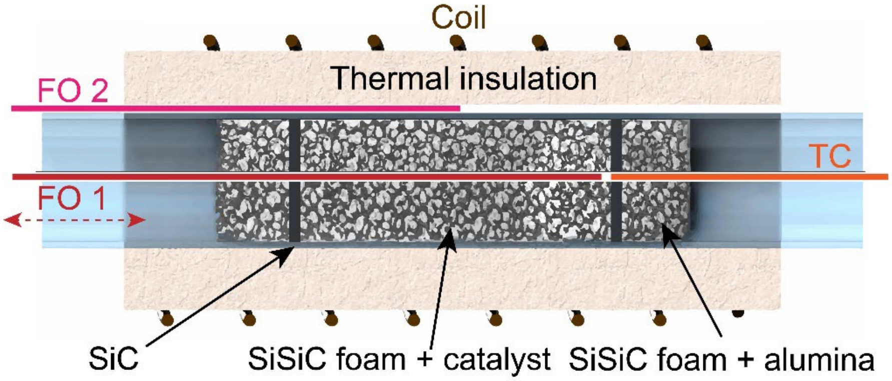

Figure S7. Schematic of our experimental temperature control and measurement configuration.

Our experimental setup is illustrated in Figure S7. To quantify the temperature profile along the symmetry axis of the cylindrical susceptor, holes in the susceptor along this symmetry axis are threaded with a silicon coated Hastelloy thermowell (Idaho Laboratories Corp.) for thermal probe placement. One probe is a K-type thermocouple located near the reaction zone outlet and is dedicated to reactor temperature control via feedback. A second probe (FO 1) is a fiber Bragg grating fiber optic (Technica) that is inserted from the inlet gas end and is axially repositioned using a translational stage (Thorlabs LTS300) to enable axial temperature measurements across a 120 mm-long reactor section. The rationale for this dual-probe arrangement is twofold: 1) The K-type thermocouple has superior stability compared to the FO probe with fluctuations of less than 0.2 °C, which is critical for stabilizing the reactor temperature; and 2) The FO probe, which consists of ceramic sensing elements, is immune to the high-frequency magnetic field and provides faster and more reliable temperature readings. To experimentally quantify radial temperature uniformity, we incorporate another ceramic FO probe (FO 2) in the middle of the reaction zone, in the narrow opening (~2 mm) between the thermal insulation and the quartz tube.

To further quantify the 3D temperature distribution within our reactor at reaction zone temperature regimes of 450 – 600 °C (i.e., our reaction temperatures), we perform steady-state multiphysics modeling that combines induction heating with heat transfer (Figure S8A). An effective medium description of the susceptor-catalyst pellet system is utilized and justified based on our analysis in Note S5. The model uses induced eddy currents as the source of joule heating, and the susceptor and coil electrical properties are consistent with those used in Note S5.

The model is configured to capture our experimental setup with high physical accuracy. The model includes a 3.25-mm diameter Hastelloy rod along the central axis of the reactor, which corresponds to the thermowell. We introduce 2-mm thermal resistance layer with a thermal conductivity of 0.06 W/(m·K) between the quartz tube and thermal insulation, which simulate imperfect thermal contact at the quartz-insulation interfaces. The thermal conductivity of the thermal insulation is set to be 0.07 – 0.11 W/(m·K) depending on the temperature, in accordance with manufacturer specifications. We set the electrical conductivity of the susceptor to be temperature-independent based on our characterization shown in Figure S2. Heat-transfer coefficients at all air-solid interfaces are set to be 20 W/(m²·K). Surface-to-ambient radiation boundaries (surface emissivity = 0.7) are also applied to all solid-air interfaces. For other material properties we used the standard values provided in the material libraries of COMSOL software.

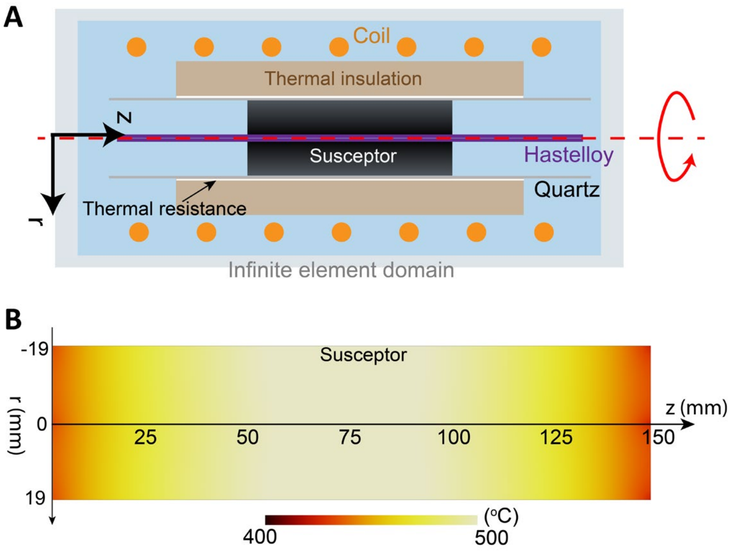

Figure S8. Multiphysics model that incorporates electromagnetics and heat transfer simulations. (A) Schematic of our two-dimensional multiphysics modeling setup. **(B)** A preliminary result that approximately estimates the axial and radial temperature distribution of the reactor.

To determine the effective thermal characteristics of our susceptor-catalyst pellet system, we conduct a parametric analysis in which we adjust the thermal conductivity of the susceptor-catalyst pellet system until the temperature profiles in the reaction zone match our experimental results. This method for determining the thermal conductivity properties of bulk heterogeneous media is standard in heat transfer studies (*S5-S7*). Data outside of the reaction zone is excluded from this process due to their high sensitivity to parameter variations. Through this analysis, we deduce that the susceptor-catalyst pellet system has an effective thermal conductivity of 16 W/(m·K). A plot of the experimental temperature profile along the symmetry axis together with the numerically simulated temperature profile with fitted thermal conduction and heat transfer parameters is shown in Figure S9A and displays good agreement.

With a fitted conductivity parameter, we numerically heat the central region of the reactor zone to 500 °C and characterize the axial and radial temperature distribution within the reactor zone. The results are summarized in Figure S9B. The radial temperature gradient across the middle of the reaction zone is minimal and is less than 3 °C. There is a more substantial temperature drop (~35 °C) at the quartz-insulation interface due to interfacial thermal resistance, which is consistent with our experimental measurements using FO 2 (see more details in Note S7). Within the central 100-mm reaction zone, the axial temperature variation is less than 40 °C, in agreement with the experimental measurements by FO 1. The axial temperature gradients at the reactor ends are attributed primarily to thermal conduction losses through the quartz tube and insulation and to convection losses.

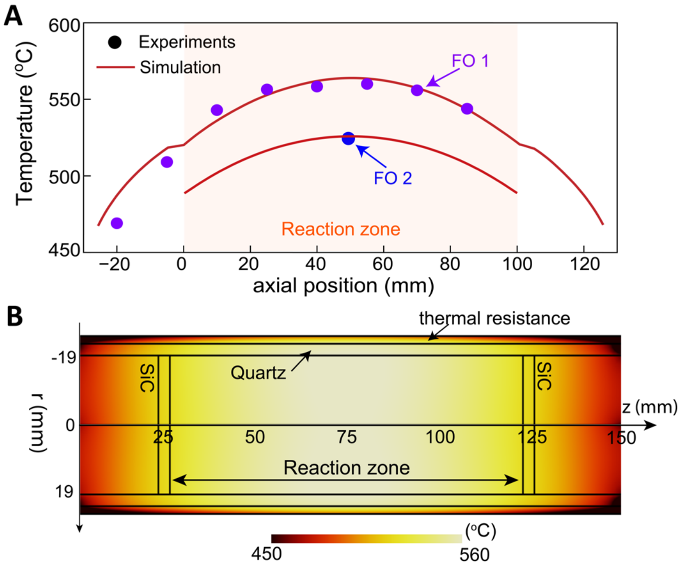

Figure S9. Comparison between simulation and experiments. (A) Experimental measurements (data points) of the axial temperature for a static state (no gas flow) with the control set to be 500 °C, accompanied by simulation fitting to the experiments (solid curves). **(B)** Simulated axial and radial temperature distribution within our reactor.

Note S7. Experimental characterization of radial temperature uniformity with gas flow and reactions

We validate the radial temperature uniformity calculated from our numerical simulations in Note S6 through experimental characterization. Furthermore, we demonstrate that the radial temperature profile is independent of gas flow rate in our range of reactor operation.

In our first set of experiments, we characterized the temperatures in the middle of the susceptor (FO 1) and at the interface between the quartz and thermal insulation (FO 2) with no gas flow (schematically shown in Figure S10A). We set the control TC to temperatures of 450°C, 500°C, 550°C, and 600°C, and monitored the temperature readings from FO probes 1 and 2. The results (square points in Figure S10B) show that the differential between the FO 1 and 2 ($\Delta T = T_{FO1} - T_{FO2}$) increases from 27°C to 33°C as the control temperature increases from 450°C to 600°C. If we consider our model in Note S6 and assume that FO 2 measures the average temperature of the outer surface of the quartz tube and inner surface of the thermal insulation, these measured temperatures by FO 2 quantitatively agreed well with our numerical model (circular points in Figure S10B). We use this agreement to validate our multiphysics model, which further specifies the temperature profile within the susceptor to be radially uniform.

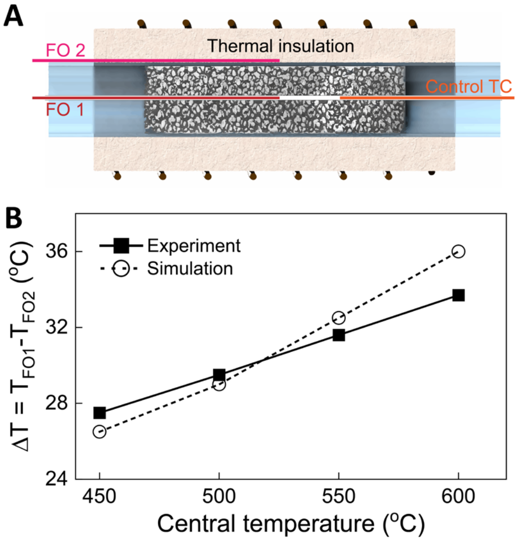

Figure S10. Experimental radial temperature uniformity characterization under static conditions. (A) Schematic of the setup in which FO 2 is placed between the thermal insulation and the quartz tube, as used in reaction experiments. **(B)** Measured ΔT (T_{FO1}-T_{FO2}) from the setup (solid square points) in (A), displaying an increase from 27°C to 33°C as control temperature increases from 450°C to 650°C. Simulated ΔT by our multiphysics model (hollow circular points) agrees well with the measurements.

In our second set of experiments, we examine the influence of gas flow on radial temperature uniformity. We used IR imaging to monitor the edge temperature (i.e., surface temperature of the susceptor) changes without the thermal insulation, as shown in Figs. S11A-B. FO 1 is used as a sensor for temperature feedback and is set to a constant temperature of 450 °C at the radial center of the susceptor, and the flow rate of nitrogen (N_2) gas is varied with gas hourly space velocities (GHSV) ranging from 0 to 8600 h^{-1}, which match the range used in our reactions. The IR camera's emissivity is calibrated and set to 0.05.

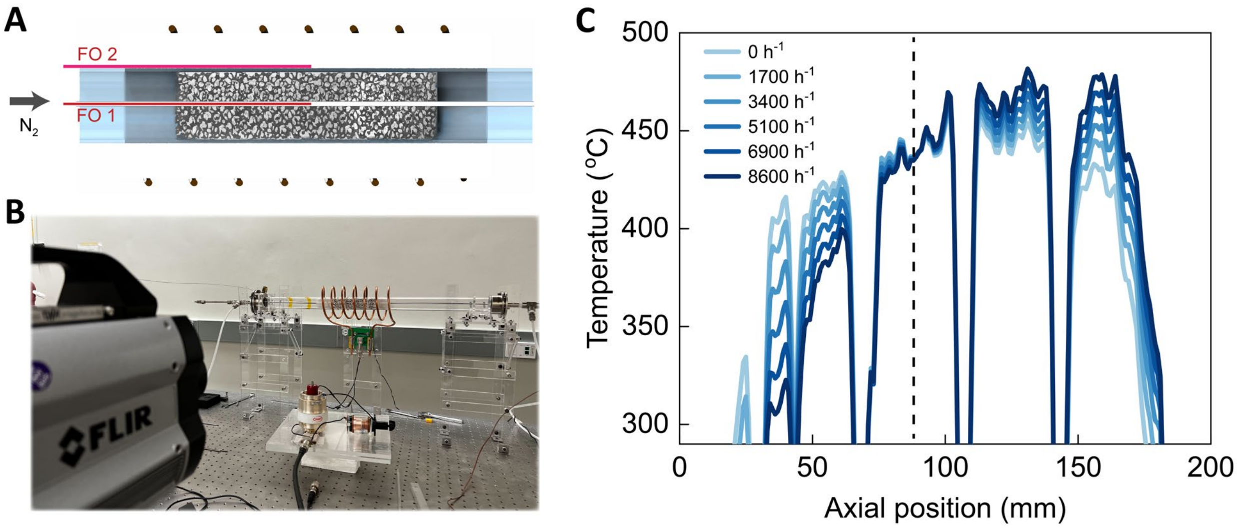

Figure S11. Investigation of the impact of gas flow on radial temperature uniformity. (A) Schematic of the experimental IR imaging setup with FO probes located inside and outside the reactor. The temperature at the center of the reactor is controlled by FO 1 at 450 °C. The surface temperature of the reactor is monitored by the IR camera and FO 2 which is attached to the outer surface of the quartz tube at the same axial position as FO 1. **(B)** Photograph of the experimental setup of (A), with the IR camera in the foreground used to monitor temperature variations on the surface of the susceptor. **(C)** Axial IR imaging temperature profile along the susceptor for gas hourly space velocities (GHSV) ranging from 0 to 8600 h^{-1}. The vertical dashed line indicates the control point maintained by FO 1.

The axial temperature distribution measured by the IR camera, shown in Figure S11C, exhibits an asymmetry (i.e., lower at the gas inlet and higher at the gas outlet) that increases with gas flow rate. However, at the axial plane at the center of the susceptor (i.e., the measuring position of FO 1), the outer surface temperature remains constant of ~450 °C and has no dependence on gas flow rate (the dashed vertical line in Figure S11C). Additionally, a second FO probe (FO 2) attached to the outer surface of the quartz tube (as shown in Figure S11A,) shows a stable temperature of approximately 397°C that is independent of gas flow rate. The relatively low temperature reading of FO 2 compared to the control temperature of 450 °C is attributed to the lack of thermal insulation and is consistent with our multiphysics modeling. With these measurements, we conclude that radial temperature uniformity within the susceptor is independent of gas flow in the gas flow regimes of reactor operation.

With this quantification of thermal gradients within the reactor system, we calibrate the radial temperature profile measurements within the reactor during operation. Recall that for the reactor experiments presented in the main text, FO 1 is situated along the axial symmetry axis of the susceptor and FO 2 is placed between the insulation and quartz tube (Figure S12A). The measured axial temperature profiles corresponding to various flow rates and reaction zone exit temperatures of 500 °C, 550 °C, and 600 °C are plotted in Figure S12B. Radial temperatures measured by FO 1 and FO 2 at the midpoint of the reaction zone are shown in Figure S12C. Using the experimental data from Figure S10 as a calibration curve and our understanding that this calibration curve is independent of gas flow, we can produce the experimental radial temperature plot within the reactor (Figure S12D, which is Figure 4D in the main text).

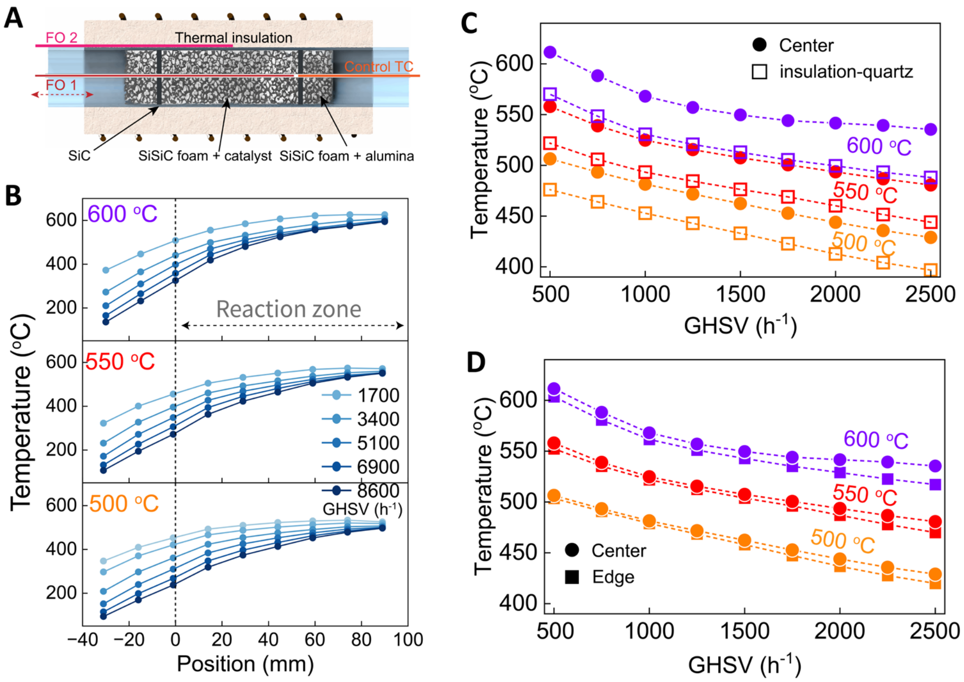

Figure S12. Axial and radial temperature measurements during reactor operation. (A) Schematic of temperature profiling setup during reactor operation. **(B)** Axial temperature distribution for exit temperatures (control TC) set at 500°C, 550°C, and 600°C for different gas flow rates. **(C)** Radial temperatures measured by FO 1 (center of the susceptor) and FO 2 (between the thermal insulation and quartz tube) at the midpoint of the reactor, across varying gas flow rates and three reaction temperatures. **(D)** Plot of temperature at the center of the reactor (measured by FO 1) and temperature at the edge of the susceptor, deduced by adding the static-state temperature drop to the FO 2 readings.

Contrary to our numerical models, we did observe slight temperature differences between the susceptor's center and edge, which could be due to the following reasons: 1) Experimental inconsistencies involving the air gap geometry between the insulation and quartz tube can exist, which can lead to a few degrees of variation between different measurement sets; 2) Reduced catalyst packing due to the combined effects of high gas flow and gravity can introduce extra thermal resistance at the interface between the susceptor and the inner quartz wall; and 3) Observed slight drifts in the FO readings over a few months of usage imply the potential for minor measurement errors inherent to the FO probes themselves.

Note S8. Systems energy balance

Power input from the DC power supply is predominantly consumed mainly through five pathways: 1) inlet gas stream heating through the addition of sensible heat; 2) heat consumed by the endothermic reaction, as quantified by the reaction enthalpy; 3) heat lost from the reactor to the environment via thermal conduction; 4) coil losses between the coil and susceptor, in which energy is dissipated by the coil; and 5) energy dissipation in the DC to MHz amplifier. We classify the first two energy consumption pathways as useful and the latter three as parasitic. Power losses due to side reactions are neglected, as justified by our experimental mass balance analysis. Power losses due to radiative heat transfer, as quantified by the Stefan-Boltzmann law, are low at our reactor temperature regime and are neglected. We write our energy balance as:

$$\text{total power } P_{tot} \approx \dot{Q}_{gas} + \dot{Q}_{react} + \dot{Q}_{cond} + P_{coil} + P_{amp} \qquad \text{(S10)}$$

Our definition of total energy efficiency is:

$$\text{total energy efficiency } \eta_{tot} = \frac{\dot{Q}_{gas}+\dot{Q}_{react}}{P_{tot}} \qquad \text{(S11)}$$

$\dot{Q}_{gas}$ and $\dot{Q}_{react}$ are directly calculated from known gas phase heat capacities and reaction enthalpies, respectively, and from experimentally measured mass flow rates and gas temperatures in the reactor. Gas heating power is given by:

$$\dot{Q}_{gas} = \sum_{i \,\epsilon\, n} F_i \cdot (H^\circ{}_i(T_{exit}) - H^\circ{}_i(T_{inlet})) \qquad \text{(S12)}$$

where F_i and $H^\circ{}_i(T)$ represent the flow rate in moles per second and the standard enthalpy of the i'th reactant, respectively. The temperature dependence of enthalpy is calculated using the Shomate equation. For these calculations, we use the experimental temperature measured by the thermocouple at the end of the reaction zone. Reaction energy consumption is calculated as:

$$\dot{Q}_{react} = F_{CO} \cdot \Delta H^\circ{}_n(T_{exit}) = F_{CO} \cdot \sum_{i \,\epsilon\, n,p} \nu_i H^\circ{}_i(T_{exit}) \qquad \text{(S13)}$$

ν_i is the stochiometric coefficient of the i'th reaction species, normalized such that $\nu_{CO} = 1$.

The power lost by the amplifier is calculated as the difference between the total power supplied by our DC power supply unit to the amplifier and the forward power at the output of the amplifier. Power dissipated in the coil is calculated from the experimental coupling efficiency based on impedance measurements and the forward power output from the amplifier. Thermal conduction power losses are experimentally quantified as the difference between the total power and other sources of energy consumption:

$$\dot{Q}_{cond} = P_{tot} - (\dot{Q}_{gas} + \dot{Q}_{react} + P_{coil} + P_{amp}) \qquad \text{(S14)}$$

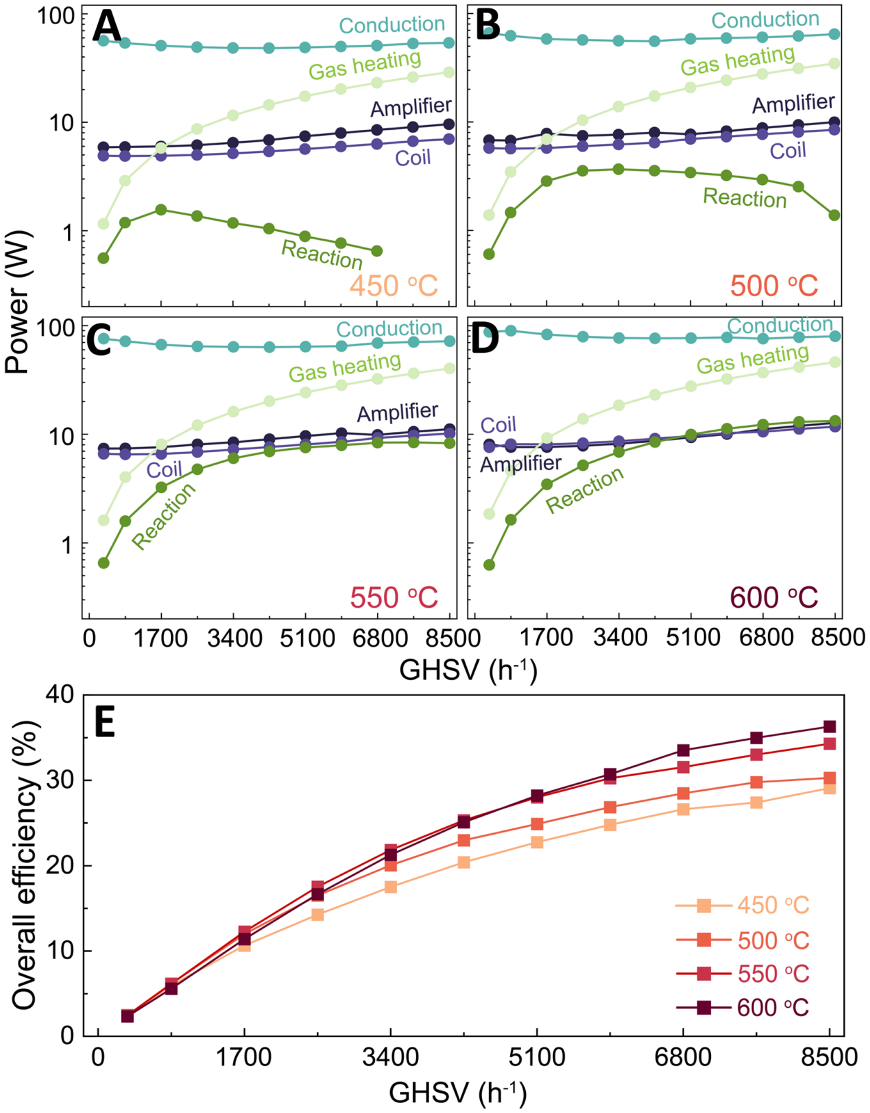

Figure S13. Experimental power consumption and energy efficiency analysis of our reactor system. (**A - D**) Experimental power consumption as a function of total input gas flow rate for different exit temperatures. Power consumption is decomposed into the five sources of power dissipation described in the text. (**E**) Total energy efficiency, specified by Eq. S11, as a function of total gas flow rate for different control temperatures.

The measured values for different power consumption pathways are displayed in Figure S13A – D. The trends are as follows. For low flow rates, we see that as the gas flow rate increases while the reaction zone outlet temperature is fixed, the thermal conduction losses decrease. This trend arises because as the gas flow rates increase, the average temperature along the length of the susceptor decreases, resulting in smaller thermal gradients across the insulation and decreased thermal losses. At higher flow rates, the power attributed to thermal conduction losses begins to increase due to enhanced heating of the susceptor end piece, which leads to enhanced conduction losses outside of the reaction zone. Coil coupling losses increase linearly with total power, and this trend follows the fact that the coil and susceptor electrical resistivities do not significantly vary in the temperature and power operating regimes of our reactor and coil. Amplifier losses scale approximately linearly with power due to its near uniform efficiency, as characterized in Note S4. The energy consumed to heat the inlet gas increases linearly with mass flow. The heat consumed by the reaction increases linearly with the product of the flow rate and conversion. Assuming near-equilibrium conversion, this trend is roughly linear with respect to flow rate.

Combining these trends together, we observe that as the process is intensified (i.e., as mass flow increases), a relatively small fraction of additional power is wasted as coupling and amplifier loss, and conduction heat losses actually decrease. As such, the total efficiency of the system increases significantly with flow rate, as observed in Figure S13E. We anticipate that further enhancements in system efficiency will be enabled by process intensification via reactor pressurization, which will be a topic of future study.

To further quantify our observed trends in conductive heat loss, we measure the power required to heat the center of the susceptor at different fixed temperatures without gas flow. We observe a nonlinear increase in the power required to sustain a given temperature, which corresponds to a linearly decreasing thermal resistance between the susceptor and ambient atmosphere outside of the reactor. We attribute this variation to the temperature dependent thermal conductivity of the insulation, which changes from 0.07 to 0.11 W/(m·K) as the temperature increases from 300 °C to 600 °C as specified by the manufacturer.

These trends match well with a simplified thermal model of our reactor system, which consists of a fixed thermal resistance between susceptor and insulation, the temperature-dependent resistance of the insulator, and a fixed resistance between the insulation and ambient atmosphere (inset of Figure S14). The first was experimentally determined as 0.5 K/W using the external FO sensor described in Note S6. We model the fixed external resistance as $R_{th} = 1/(2\pi h R_{reactor} L_{eff})$, where h is the heat transfer coefficient (approximately 20 W/(m^2·C)), $R_{reactor}$ is the radius of the reactor, and L_{eff} is the effective length of the region dissipating heat. To model the insulation, we begin with the thermal shape factor of a hollow cylinder $S = \frac{\ln(r_o/r_i)}{2\pi k L_{eff}}$ where r_o and r_i are the outer and inner radii of the cylinder respectively, with thickness t_{ins} [S9]. Taking the limit of $r_o \to r_i + dr$, we find $dR_{th} = \frac{dT}{\dot{Q}} = \frac{dr}{2\pi k L_{eff} r}$. Here, the thermal conductivity, k, is implicitly a function of temperature: $k = k(T)$. We model this using a quadratic fit to the vendor's data ($k(T) = \alpha T^2 + \lambda T + \gamma$), which does not include any data less than 300 °C and therefore may not apply at low temperatures. With this, we can write:

$$\int_{T_i}^{T_o} k(T) dT = \int_{r_i}^{r_o} \frac{\dot{Q}}{2\pi L_{eff} r} dr \qquad \text{(S15)}$$

$$\to \dot{Q} = \frac{2\pi L_{eff}}{\ln(r_o/r_i)} \int_{T_i}^{T_o} k(T)\, dT \qquad \text{(S16)}$$

where $k(T)$, expressed as a quadratic, is simple to integrate. Finally, we choose L_{eff} such that the temperature drop across the three resistors matches the difference between our susceptor and ambient temperature. We find effective lengths ranging from 240 to 260 mm between 150 °C to 650 °C, which is in reasonable agreement with the 150 mm length of our susceptor given axial heat spreading. This calculation also yields an insulation surface temperature of 61 °C when the susceptor is at 500 °C, which is in good agreement with the 46 - 69 °C surface temperature values experimentally measured across a 250 mm-wide region of the insulation centered at the reaction zone. For a given temperature, this model yields a cubic function, the root of which is the power required to sustain the input power. The results are plotted in Figure S14. This model reproduces the experimental data well across a broad temperature range with a simple linear fit of $L_{eff}(T)$.

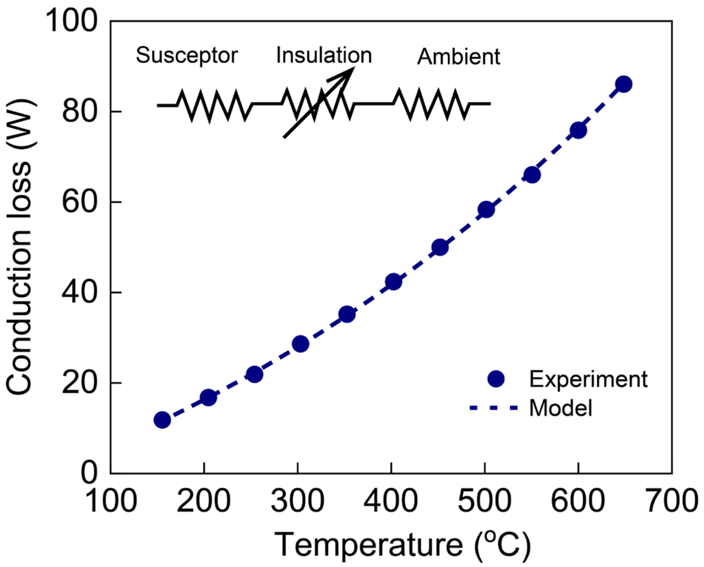

Figure S14. Conduction loss measurements and modeling as a function of temperature.

Note S9. Reactor scale up analysis

We extend the analysis from Note S8 to larger reactor sizes and show that the total energy efficiency increases with reactor scaling. We start with a base reactor case that involves our 38 mm diameter reactor operating with an outlet temperature of 550°C and a gas hourly space velocity (GHSV) of 1700 h^{-1}. At these conditions, CO_2 conversion near equilibrium is achieved, as shown in Figure 4E in the main text. We consider this specific operating condition because conversion at this mass flow is robust to minor variations in the reactor temperature profile, leading to a simplified and more robust scale up analysis. We consider the scaling of each linear dimension of the reactor (i.e., diameter and height) by a factor β, and the scaling of gas flow rates such that the mass flow per unit of reactor volume is constant. We assume that volumetric power delivery produces radially uniform temperature profiles, yielding ideal plug flow reaction conditions and conversion near equilibrium. To ensure that the heating profile within the reactor properly scales with reactor size, the skin depth of our susceptor must scale accordingly, yielding: $(\sigma_{eff} f)^{-1/2} \propto R_{reactor}$. For this analysis, we fix frequency and scale the susceptor effective conductivity accordingly.

Having set up our scaling assumptions, we next discuss the power consumption scaling trends of our reactor system. Increases in every dimension of our reactor by β results in a reaction volume increase by a factor of β^3 and a gas flow increase by a factor of β^3. Since all gases heat to an exit temperature of 550 °C, the energy consumed by gas heating scales as β^3. Our assumption of equilibrium conversion implies the reaction power also scales as β^3. We therefore have:

$$\dot{Q}_{gas} = \beta^3 \dot{Q}^0_{gas} \quad \text{(S17)}$$

$$\dot{Q}_{react} = \beta^3 \dot{Q}^0_{react} \quad \text{(S18)}$$

Expressions with superscript 0 denote powers measured for our base case. Similarly, we consider a scaled version of the conduction model described in Note S8 for thermal conduction losses. We scale the insulation thickness by β, from which the effective length, the inside insulation, and the outside insulation all scale as β. We also explicitly scale the susceptor-to-insulator thermal resistance as β^{-2} given the increased surface area. The insulation-to-ambient resistance scales in the same way. In summary:

$$\dot{Q}_{cond} = \dot{Q}_{cond}(L_{eff}, r_i, t_{ins}, R_{th}) = \dot{Q}_{cond}(\beta L^0_{eff}, \beta r^0_i, \beta t_{ins}, \beta^{-2} R^0_{th}) \quad \text{(S19)}$$

Next, we consider current and power scaling in the induction coil. We assume that the coil diameter is specified such that the inner coil surface is 10 mm away from the insulation, and that it axially extends past the susceptor by a length of $2r_i$ at each end. Using the expressions from Note S2, we observe that at fixed current, the power delivered to the susceptor scales as β^3: $P_{susc}(I^0_{coil}) = \beta^3 P^0_{susc}(I^0_{coil})$. Furthermore, the delivered power scales as I^2_{coil}. For $P_{susc} = \dot{Q}_{gas} + \dot{Q}_{react} + \dot{Q}_{cond}$ defined to be the total heat delivered to the susceptor, we can get:

$$I_{coil} = \sqrt{\frac{P_{susc}}{\beta^3 P^0_{susc}}} I^0_{coil} \quad \text{(S20)}$$

The power dissipated in the coil is given by $I^2_{coil} R_{coil}$. Its resistance is linear with respect to the total coil length, L_{coil}, which scales approximately as $(L_{susc} + 4R_{susc}) \cdot r_{coil} = \beta(L^0_{susc} + 4R^0_{susc}) \cdot (r_i + t_{ins} + 0.01m)$. In total, the power dissipated in the coil scales as:

$$P_{coil} = \left(\frac{I_{coil}}{I_{coil}^{0}}\right)^{2} \left(\frac{R_{coil}}{R_{coil}^{0}}\right) P_{coil}^{0} = \frac{P_{susc}}{\beta^{3} P_{susc}^{0}} \cdot \frac{\beta(r_i + t_{ins} + 0.01m)}{(r_i^{0} + t_{ins}^{0} + 0.01m)} P_{coil}^{0} \quad \text{(S21)}$$

Finally, we take the amplifier efficiency to be a constant value of 92.8%, which corresponds to the lowest efficiency observed in our experiments. As such, power dissipated in the amplifier scales as:

$$P_{amp} = (\dot{Q}_{gas} + \dot{Q}_{react} + \dot{Q}_{cond} + P_{coil}) \cdot \left(\frac{1}{0.928} - 1\right) \text{(S22)}$$

The power breakdown for several scale factors are shown Table S1, and the efficiencies as a function of reactor diameter are shown in Figure S15. We observe good agreement between our base case and its corresponding simulation, with total energy efficiencies of 12.3 and 12.7%, respectively. We observe that the assumed useful power of $\dot{Q}_{gas} + \dot{Q}_{react}$ scaling as β^3 allows it to quickly dominate system inefficiencies, which mostly scale as β^n where n is less than 3 (see details in Table S1).

Physically, the useful power delivered to the reactor (both gas heating and reaction) is proportional to the volume of the reactor which scales as the cube of length. The surface area of the reactor increases only as the square of the length while the insulation grows thicker linearly in length; the combination of these factors results in conduction losses that scale with a power law dependence which are less than that for useful power. Similarly, with a fixed magnetic field amplitude, the power delivered to the susceptor will scale with the susceptor volume. This constant amplitude can be achieved with fixed current by increasing coil radius and length to accommodate the larger susceptor, resulting in a quadratic length increase and therefore quadratic power dissipation increase. Again, this implies that coil losses become negligible in a sufficiently large system. Lastly, amplifier losses represent a fixed fraction of the total delivered power, setting the limit on system efficiency. This limit is practically reached once our reactor scales to > 0.5m in diameter, at which point the overall efficiency is within 1% of the amplifier efficiency, and we conclude our scaling analysis at this point.

Table S1. Reactor dimensions, power dissipation, and total energy efficiency as a function of reactor scaling.

	R_{susc}	L_{susc}	$\dot{Q}_{gas}$	$\dot{Q}_{react}$	$\dot{Q}_{cond}$	P_{coil}	P_{amp}	η
Unit	m	m	W	W	W	W	W	%
Base (exp.)	0.019	0.15	8.08	3.38	69.3	6.08	6.06	12.3
β=1	0.019	0.15	8.08	3.38	66.5	5.86	6.50	12.7
β=2	0.038	0.30	64.63	27.05	135.7	7.57	18.23	36.2
β=4	0.076	0.60	517.1	216.4	274.4	15.71	79.41	66.5
β=8	0.152	1.20	4137	1731	552.0	48.31	501.8	84.1
β=16	0.305	2.40	33090	13847	1107	177.6	3742	90.3
Scaling	β	β	β^3	β^3	$\sim\beta$	$\sim\beta^2$	$\sim\beta^3$	$\rightarrow \eta_{amp}$

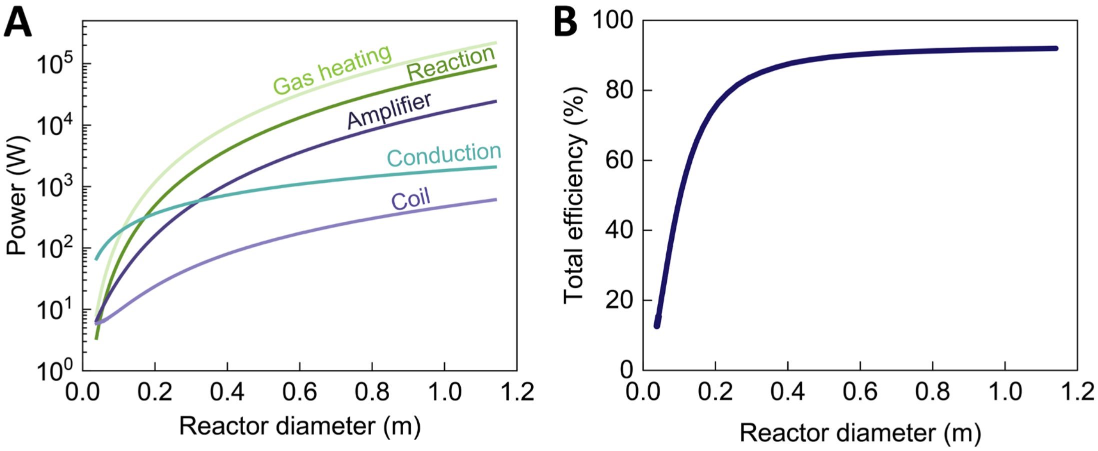

Figure S15. Power dissipation and total energy efficiency as a function of reactor size. (A) Plot of power dissipation as a function of reactor diameter, decomposed into the five power dissipation pathways described in Note S7. The reaction, gas heating, and power amplifier losses scale cubically as a function of reactor diameter and dominate power consumption in scaled reactor systems. **(B)** Plot of total energy efficiency as a function of reactor diameter. The energy efficiency of the reactor approaches the efficiency of the amplifier upon scaling.

To verify the constant conversion approximation, we consider the characteristic numbers describing flow regimes, heat transfer, and mass transfer in our system. To begin with, we calculate the pore Reynolds number as 0.4 in our base case[S10]. While it will scale linearly with beta due to increasing gas flow velocity, it remains well in the laminar regime for all scales considered here. We next consider the Peclet and Prandtl numbers describing local mass and heat diffusion in the pores respectively[S11]. With formulas of

$$\mathrm{Pe_T} = \frac{\mathrm{p^2/D}}{\mathrm{L/u}} \ \& \ \mathrm{Pr_T} = \frac{\mathrm{p^2/k}}{\mathrm{L/u}} \sim \beta^0 \qquad \text{(S23)}$$

where p is the pore diameter, D is the diffusivity of the gas species, k is the thermal conductivity, L is the susceptor length, and u is the mean gas velocity, we observe that these values remain constant under our scaling assumptions. The reactor-scale transverse Peclet and Prandtl numbers are irrelevant under the assumption of well mixed gases and radially uniform heating. The axial Peclet and Prandtl numbers of the form $PE = (L^2/D)/(L/u)$ scale as β^2 due to increasing length and fluid velocity, hence further validating the plug flow assumption. Finally, we expect Nusselt and Sherwood numbers to remain constant, as the structure is identical at the relevant length scales.

The analysis presented here is based on simplifications and assumptions that do not lead to optimal total energy efficiencies in scaled systems. For example, a non-linear scaling of insulation thickness, in a manner that optimally trades off coupling efficiency with conduction loss, would lead to further improvements to conduction loss scaling. In another example, the coil geometry itself could be further optimized upon scaling. Ultimately, a more detailed co-optimization of material, metamaterial geometry, induction frequency, and electronics is required to account for pressure drop, temperature uniformity, EMI regulations, and high-power DC/AC conversion considerations. Such an analysis will be the topic of future study.

In a practical application, an induction heated metamaterial reactor would be integrated into a heat management system including features such as countercurrent heat exchangers to recover a portion of the sensible heat added to the gases and ensure a more uniform axial temperature profile. To account for this scenario, we consider a separate scaling analysis in which the gas inlet and outlet temperatures are both set at 550 °C. We assume this would result in a uniform axial profile to simplify analysis, although in practice the temperature will drop somewhat near the inlet due to increased energy consumed by reaction there. Under our plug flow model (see Note S11), this temperature profile would allow us to increase the GSHV to 4760 hr^{-1} while maintaining a conversion within 1% of equilibrium. We then perform an identical scaling analysis considering only power consumed by the reaction. We observe that while the efficiency is slightly worse in this scenario, the difference is negligible, and all previous observations hold. Further, we anticipate that a combination of pressurization and improved catalytic activity could enable higher flow rates without a loss in conversion. In this regime, the power demands to drive the endothermic reaction could be increased to the megawatt scale. Such an application would still take full advantage of the volumetric heating capability, simple implementation, and scalability of this work. We note that metallurgical heating systems give precedent for induction heating systems of such size, with current metallurgical induction furnace installations reaching tens of megawatt power levels.

Finally, the high heat transfer rates enabled by our large surface area baffle would generally enable heating systems that efficiently deliver heat to fluids. We anticipate that our concept can be readily adapted to the heating a heat transfer fluid such as pressured steam, for use in existing heat-exchanger based reactors, or as a gas preheater for adiabatic flow reactors.

Note S10. Supplementary information on RWGS reactions

Note S10.1 Catalyst preparation and characterization

Spherical γ-Al_2O_3 pellets (1-1.4 mm in diameter, supplied by Shanghai Guangji Industry) were used as the catalyst support. These pellets were sieved to ensure uniform size distribution and pretreated with a calcination step at 650 °C for 3 hours. Incipient wetness impregnation was used to impregnate K_2CO_3 (Alfa Aesar) into the support. In this step, a total of 100 g of pellets was placed in a glass container and a 3.92 M aqueous K_2CO_3 solution was incrementally added. During the impregnation process, the mixture was stirred gently to ensure even distribution. After impregnation, the catalyst was left to stand at room temperature overnight, followed by drying under vacuum at 150°C for 1 hour. The resultant catalyst had a K_2CO_3 loading of 18.1 wt%.

The pore characteristics of the support is determined using an Anton Paar NovaTouch surface area and pore size analyzer. Approximately 150 mg of the pellets are placed into a pre-weighed glass cell and sealed with a rubber ring. The cell is subjected to vacuum drying at 300 °C for a minimum of 3 hours to remove any moisture. Then, the evacuated cell is weighed, and the initial cell weight is deducted to ascertain the precise mass. The sample was characterized using the BET method and N_2 adsorption isotherms at 77 K with a BET relative pressure (P/P_0) range of 0.05 to 0.3. The specific surface area was characterized to be 306.3 m^2/g. A pore volume of 0.407 cc/g was calculated using the Barrett-Joyner-Halenda (BJH) method based on the N_2 adsorption data at 77 K.

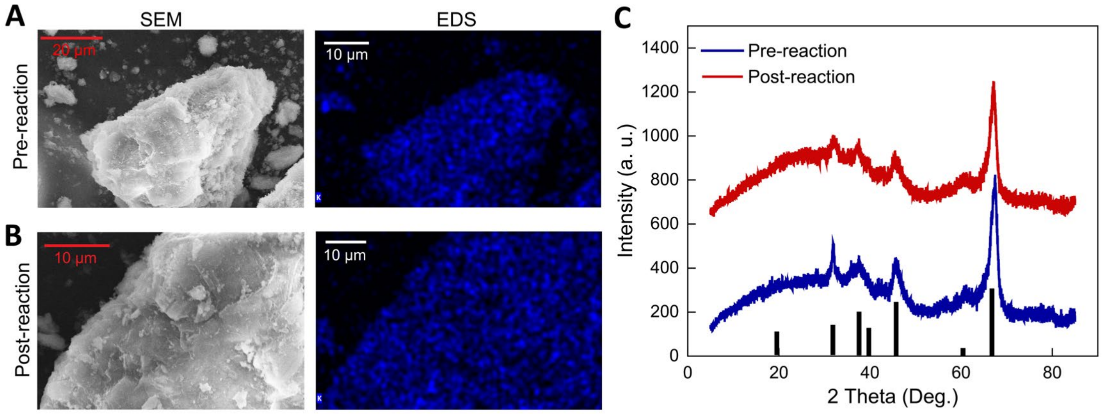

Figure S16. Catalyst characterization before and after the reaction. (A) SEM and EDS images of fresh catalyst before reaction. **(B)** SEM and EDS images of catalyst after the reaction. **(C)** XRD analysis of catalyst power before and after reaction.

The morphology of fresh and spent catalyst particles and the distribution of potassium carbonate on the supports is characterized using scanning electron microscopy (SEM, Thermo Fisher Scientific Apreo S LoVac) and energy-dispersive X-ray spectroscopy (EDS), respectively. Prior to analysis, the catalyst particles are ground into a fine powder. As shown in Figure S16A-B, the morphology of the catalyst remained consistent before and after the reaction, with potassium uniformly distributed across the support surface.

Powder X-ray diffraction (PXRD, PANalytical Empyrean) is employed to investigate crystallinity, operating with a copper source (Cu Kα radiation, 8.04 keV) at conditions of 45 kV and 40 mA. The diffractograms (Figure S16C) indicate that the crystal structure of the catalyst remains unchanged pre- and post-reaction. The major diffraction peaks are consistent with the crystalline alumina, as indexed in the HighScore dataset.

K_2CO_3 stays in the amorphous phase, as indicated by the absence of diffraction peaks attributable to crystalline K_2CO_3.

Note S10.2 Reaction data analysis

In our experiments, Ar (Linde Gas & Equipment Inc., purity 99.995%) was used as carrier gas with inlet gases CO_2 (Linde Gas & Equipment Inc., purity 99.995%) and H_2 (Praxair/Linde Gas, purity 99.995%). The mass spectrometer was used for analyzing concentrations of CO, CO_2, H_2 and Ar. The CO_2 conversion was calculated using following methods:

$$CO_2\ conversion = \left(1 - \frac{f_{Ar} C_{CO_2}}{C_{Ar} f_{CO_2}}\right) \times 100\% \quad \text{(S24)}$$

$$Carbon\ element\ balance = \left(\frac{f_{Ar}(C_{CO_2} + C_{CO})}{C_{Ar} f_{CO_2}}\right) \times 100\% \quad \text{(S25)}$$

Where f_{Ar}, f_{CO_2} are inlet gas flow rate of Ar and CO_2, C_{Ar}, C_{CO_2}, C_{CO} are measured gas concentrations of Ar, CO_2 and CO from the mass spectrometer. Carbon element balance during the reaction was close to 100%, indicating CO is the only carbon product.

Total flow rate in the experiment was 1-5 SLPM. The volume of catalyst particles we used is 34 mL. The corresponding GHSV can be calculated as:

$$GHSV = \frac{flow\ rate * 60\ min/h}{catalyst\ volume} \quad \text{(S26)}$$

We estimated the uncertainty CO_2 conversion via repeated trials and identified a standard deviation of approximately 1.6%. Fiber optic temperature measurement error comes from two sources: random variation and drift of the spectrum of the sensor. We assume the former is gaussian, and repeated trials identified a standard deviation of 0.6°C for both sensors. This variation is independent for each measurement. Further, the spectrum of the center sensor (i.e. FO 1) drifted the equivalent of 7°C between two calibrations performed before and after the experiments, bounding the error caused by the drift. This variation is highly correlated between successive measurements, although we do not know the amount of drift at the time of the experiment.

Pressure drop analysis

Pressure drop tests were performed using the same GHSV range, 1700-8600 h^{-1}, as used in our reactions, corresponding to a superficial velocity of 0.015-0.075 m/s. The test was conducted by flowing nitrogen at room temperature with a differential pressure gauge (Omega PX419-005DWU5V) measuring the pressure drop across the reactor tube, for three cases: empty SiSiC foam, SiSiC foam packed with alumina particles, and a column of closely packed alumina particles of equivalent length. The pressure drop of an empty tube was used as the baseline. These pressure drop measurements were performed with thin (6.3mm, 100PPI) SiC foam disks on either end of the foam. The SiC disks were used to hold the packed particles in place in a horizontal reactor, as in our reactions. We observed that the contribution of the SiC disks to the overall pressure drop was constant and negligible across each test.

For each of the three cases, the pressure drop per unit length was fitted using the Forchheimer equation[S12,S13]:

$$\frac{\Delta P}{L} = \frac{a\,\mu\,v}{d_p^2} + \frac{b\,\rho\,v^2}{d_p} \quad \text{(S27)}$$

Where ΔP is packed bed pressure drop, L is the packed bed length, a and b are fitting coefficients, μ is the dynamic viscosity of the gas, v is the superficial velocity, d_p is the particle diameter, ρ is the gas density.

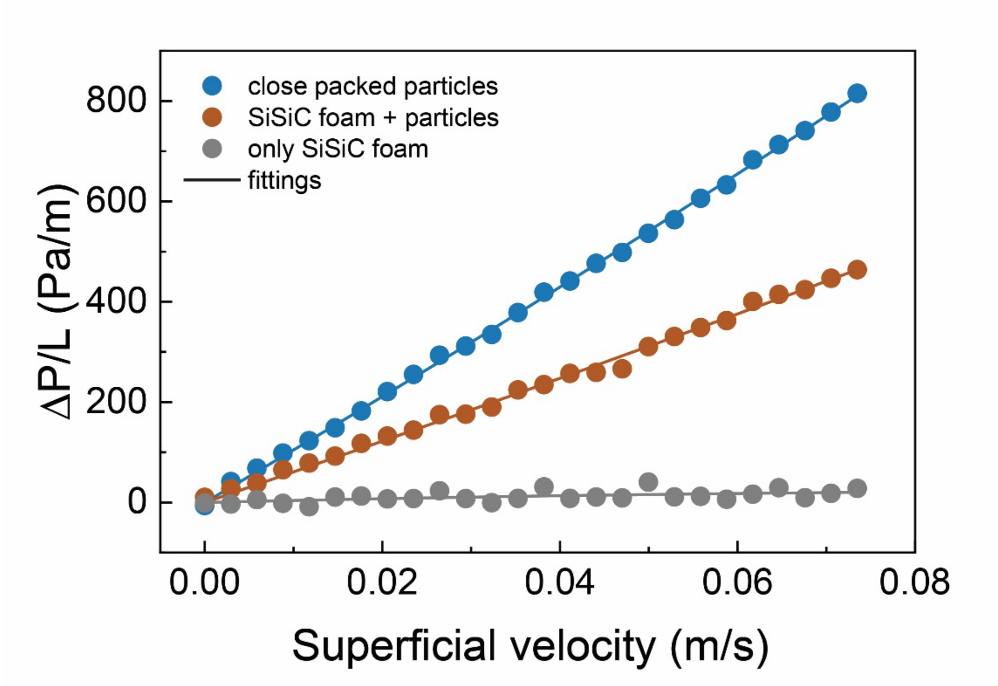

Figure S17. Measured pressure drop in our reactor setup as a function of superficial velocity. Standard deviation of all measurements is about ± 1%.

The results are plotted in Figure S17. For catalyst particles packed with SiSiC foam, a is at 345 and b is at 3.0, with $R^2 = 0.99$. For the packed bed system with only catalyst particles, a is at 593 and b is at 7.3, with $R^2 = 1.00$. We observe that the packing of catalyst particles with the SiSiC foam leads to reduced pressure drop, likely due to wall effects and the presence of added void spaces at the foam wall.

Note S10.3 Stability tests

Alumina, SiC, SiSiC, and quartz have thermal expansion coefficients that are approximately 8.1 $\times 10^{-6}$ /°C, 4.0 $\times 10^{-6}$ /°C, 4.5 $\times 10^{-6}$/°C, and 0.55$\times 10^{-6}$/°C, respectively[S14,S15,S16,S17]. These values are similar and relatively low, enabling reactor system heating with minimal mechanical stress. Furthermore, the particles are packed in the SiSiC foam, rather than washcoated or chemically bonded, eliminating issues involving the debonding of catalyst materials from the monolith.

To further characterize the mechanical and performance stability of our reactor system, we ran the RWGS reaction continuously for an 80-hour run and additionally ran the reactor in a temperature cycled configuration. For the continuous run, the reaction was performed at 500°C with a gas mixture molar ratio H_2:CO_2:Ar = 3:1:1 and a flow of GHSV = 2700 h^{-1}. The results are shown in Figure S18A and indicates that our reaction remains stable over the full timespan. The conversion drifting over time is primarily due to drift in the mass spectrometer reading arising from hydrogen accumulation. For the cycling experiment, a high power of ~350 W is applied to quickly heat the reactor to a reaction temperature of 500 °C, followed by lowering of the temperature to 100°C. The cycling test results (Figure S18B) show that CO_2 conversion did not degrade upon cycling and that we are able to ramp the reactor temperature from 100 to 500 °C in approximately ten minutes. Both of the tests show no signs of degradation in performance.

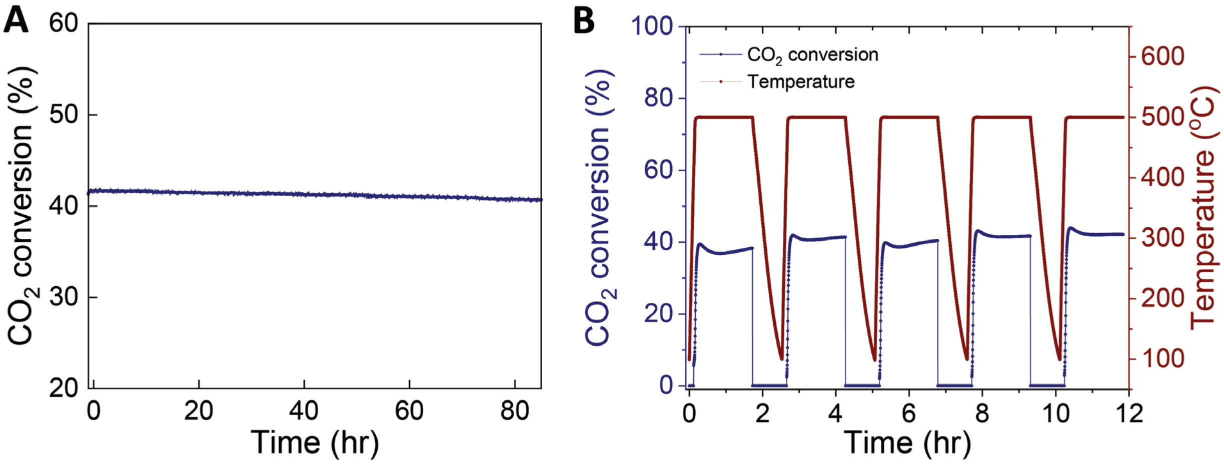

Figure S18. Stability tests of our reactor system. (A) Plot of CO_2 conversion as a function of time for an 80-hour reaction run. **(B)** Plot of CO_2 conversion as a function of time for the reactor programmed to undergo cycling between high (500 °C) and low (100 °C) temperatures.

Note S11. 1D plug flow model of reaction conversion with axial temperature variations

We model our reactor in the ideal plug flow limit. At steady state, mass balance is expressed as[S18]:

$$F_i(z) - F_i(z + dz) + Av_i r(C, T)dz = 0 \qquad \text{(S25)}$$

Here z is the reactor tube axial position, dz is the differential thickness of fluid plug, i indexes the species, $F_i(z)$ is the molar flow rate of species *i* at the position z, A is the tube transverse cross sectional area, v_i is stoichiometric coefficient of species *i*, and $r(C, T)$ is the concentration and temperature dependent reaction rate. Molar flow rate relates to concentration as $F_i = AC_i u(T)$, where $u(T) = u(STP) \cdot \frac{T}{273.15}$ is the temperature-dependent linear flow rate. $u(STP)$ is calculated using the ideal gas law and our given mass flow. With these terms, we write the differential equation:

$$\frac{dC_i}{dz} = \frac{v_i r(T,C)}{u(T)} - \frac{C_i}{T}\frac{dT}{dz} \qquad \text{(S26)}$$

To calculate conversion with this model, we integrate this equation using our input reactant concentrations as initial conditions and the experimentally measured temperature profiles with FO 1 as the axial temperature profile. A continuous temperature profile is constructed from the discrete experimental profile using linear interpolation.

The rate expressions for the forward and reverse reactions are assumed to be elementary, which is consistent with many reaction models for RWGS catalysts[S19]:

$$k_f = A_f[CO_2][H_2]\exp\left(-\frac{E_{a,f}}{R_{gas}T}\right) \qquad \text{(S27)}$$

$$k_r = -A_r[CO][H_2O]\exp\left(-\frac{E_{a,r}}{R_{gas}T}\right) \qquad \text{(S28)}$$

A_f, A_r, $E_{a,f}$, and $E_{a,r}$ are not independent but must relate in the following way at equilibrium due to thermodynamics:

$$\frac{[CO][H_2O]}{[CO_2][H_2]} = K = \exp\left(-\frac{\Delta G°}{R_{gas}T}\right) \qquad \text{(S29)}$$

Thus, at equilibrium:

$$k_f = -k_r \rightarrow \frac{A_f}{A_r}\frac{1}{K}\exp\frac{E_{a,r} - E_{a,f}}{R_{gas}T} = \frac{A_f}{A_r}\exp\frac{\Delta G°}{R_{gas}T}\exp\frac{E_{a,r} - E_{a,f}}{R_{gas}T} = 1 \qquad \text{(S30)}$$

We note that $\Delta G°(T)$ is approximately linear over the temperature range of interest, and we expand $\Delta G°(T) \approx \Delta G_0 + \Delta G'T$. With this approximation, to ensure the above expression has no temperature dependence we find:

$$E_{a,r} - E_{a,f} = -\Delta G_0 \qquad \text{(S31)}$$

$$A_r = A_f \exp\left(\frac{\Delta G'}{R_{gas}}\right) \qquad \text{(S32)}$$

Thus, equilibrium conditions reduce our four parameter model to a two parameter model involving A_f and $E_{a,f}$, which we use as fitting parameters.

To extract these parameters, we begin by approximating a covariance matrix for our system. We expect the variances in conversion for two given flow rates to be similar, and likewise for covariances in conversion between sets of flow rates. As such, we assume a covariance matrix with one value for all the diagonal entries, and a second for all off diagonal entries. Repeated experiments in a similar setup identified variances of 0.000265, corresponding to a standard deviation of 1.63%, and covariances of 0.000213, corresponding to a correlation of 0.804. These variances are likely due to some combination of mass spectrometer measurement error, temperature measurement error, variation in catalyst performance, variation in catalyst packing, and variation in catalyst surface area.

Next, we determined our parameters as the set which minimized the X^2statistic given by $(\vec{x}-\vec{\mu})^T\Sigma^{-1}(\vec{x}-\vec{\mu})$, where $\vec{x}$ is the measured conversions, $\vec{\mu}$ is the conversion predicted by our plug-flow model with the given A_f and $E_{a,f}$, and Σ^{-1} is the inverse of the covariance matrix. Gradient descent yields optimal A_f at $1.12 \times 10^7 \frac{m^3}{mol \cdot s}$ and $E_{a,f}$ at $120 \frac{kJ}{mol \cdot K}$ and yields $\mathrm{X}^2 = 24.76$, which corresponds to a significance of 0.82. As this is less than the commonly accepted significance level of 0.95, we determine that our dataset is consistent with plug flow operation with the specified rate equations.

Note S12. Table of Variables

Table S2. Table of variables

Symbol	Description	Unit
R	Radius of reactor	mm
d	Skin depth	m
μ_0	Magnetic permeability of free space	$4\pi \times 10^{-7}$ H/m
f	Frequency	Hz
w	Angular frequency	Rad/s
σ_{eff}	Effective electrical conductivity	S/m
σ_0	Intrinsic material electrical conductivity	S/m
e	Porosity	
t	Tortuosity	
b	Scaling factor	
B_0	Magnitude of imposed magnetic field	T
r, z, f	Cylindrical coordinates (radial, axial, angular position)	m, m, rad
B_e	Magnitude of induced magnetic field	T
J_0, J_2	Bessel function of the 0th and 2nd order	
$\mathbf{J}$	Current Density	A/m^3
L	Length of susceptor/coil	m
L_{eff}	Effective length	m
P	Power	W
N	Number of coil turns	
I	Root mean square of coil current	A
R_{susc}	AC Resistance of susceptor	W
R_{coil}	AC Resistance of coil	W
$h_{coupling}$	Coupling efficiency	%
s_c	Electrical conductivity of copper coil	S/m
d_c	Skin depth of copper coil	m
R_c	Radius of copper tube	m
d	Diameter of coil	M
R_{th}	Thermal resistance	K/W
T	Temperature	°C
$\dot{Q}$	Heat transfer rate	W
h_{tot}	Total efficiency	%
F	Molar flow rate	mol/s
H°	Standard enthalpy	J/mol
h	Heat transfer coefficient	W/(m^{2}K)
k	Thermal conductivity	W/(m^{2}K)
k_f	Forward rate constant	
k_r	Reverse rate constant	
K	Equilibrium constant	
k	Complex wavenumber	m^{-1}
r_i	Insulation inner radius	m
r_o	Insulation outer radius	m
t_{ins}	Insulation thickness	m
T_i	Insulation inner temperature	°C
T_o	Insulation outer temperature	°C
p	Pore diameter	m
S	Shape factor	
a, l, g	Quadratic fitting parameters	
f_{Ar}	Argon flow rate	L/min
f_{CO2}	Carbon dioxide flow rate	L/min

C	Concentration	mol/m^3
$r(C,T)$	Reaction rate	mol/(m^{3}s)
u	Volumetric flow rate	m^3/s
n	Stoichiometric coefficient	
A	Cross-sectional area	m^2
DG°	Standard Gibbs free energy	J
A_f	Forward pre-exponent constant	
A_r	Reverse pre-exponent constant	
$E_{a,f}$	Forward activation energy	J
$E_{a,r}$	Reverse activation energy	J
R_{gas}	Gas constant	8.314 J/mol
D	Diffusivity	
Subscripts		
diss	Dissipation	
FO1	First Fiber Optic	
FO2	Second Fiber Optic	
gas	Gas	
react	Reaction	
cond	Conduction	
amp	Amplifier	
CO	Carbon Monoxide	
CO_2	Carbon Dioxide	
Ar	Argon	
i	i-th reactant (or i-th species)	
n	Total number of reactants	
Superscripts		
0	Base case	
Abbreviations		
SCCM	Standard cubic centimeter per minute	cm^3/min
RWGS	Reverse water gas shift	
GHSV	Gas hourly space velocity	h^{-1}
SLPM	Standard liter per minute	L/min

Supplemental references

[S1]. Bidinosti, C.P., Chapple, E.M., and Hayden, M.E. (2007). The sphere in a uniform RF field - Revisited. Concepts in Magnetic Resonance Part B: Magnetic Resonance Engineering *31*, 191–202. https://doi.org/10.1002/cmr.b.20090.

[S2]. Nagel, J.R. (2017). Induced Eddy Currents in Simple Conductive Geometries Due to a Time-Varying Magnetic Field. IEEE Antennas and Propagation.

[S3]. Nan, X., and Sullivan, C.R. (2003). An improved calculation of proximity-effect loss in high-frequency windings of round conductors. In IEEE 34th Annual Conference on Power Electronics Specialist, 2003. PESC '03., pp. 853–860 vol.2. https://doi.org/10.1109/PESC.2003.1218168.

[S4]. ACDCModuleUsersGuide.pdf.

[S5]. Cuevas, F.G., Montes, J.M., Cintas, J., and Urban, P. (2009). Electrical conductivity and porosity relationship in metal foams. J Porous Mater *16*, 675–681. https://doi.org/10.1007/s10934-008-9248-1.

[S6]. Bianchi, E., Schwieger, W., and Freund, H. (2016). Assessment of Periodic Open Cellular Structures for Enhanced Heat Conduction in Catalytic Fixed-Bed Reactors: Heat Conduction in Periodic Open Cellular Structures. Adv. Eng. Mater. *18*, 608–614. https://doi.org/10.1002/adem.201500356.

[S7]. Bianchi, E., Heidig, T., Visconti, C.G., Groppi, G., Freund, H., and Tronconi, E. (2013). Heat transfer properties of metal foam supports for structured catalysts: Wall heat transfer coefficient. Catalysis Today *216*, 121–134. https://doi.org/10.1016/j.cattod.2013.06.019.

[S8]. Bracconi, M., Ambrosetti, M., Maestri, M., Groppi, G., and Tronconi, E. (2018). A fundamental analysis of the influence of the geometrical properties on the effective thermal conductivity of open-cell foams. Chemical Engineering and Processing - Process Intensification *129*, 181–189. https://doi.org/10.1016/j.cep.2018.04.018.

[S9]. Hirbodi, K., and Jafarpur, K. (2020). A simple and accurate model for conduction shape factor of hollow cylinders. International Journal of Thermal Sciences *153*, 106362. https://doi.org/10.1016/j.ijthermalsci.2020.106362.

[S10]. González-Neria, I., Yáñez-Varela, J.A., Martínez-Delgadillo, S.A., Rivadeneyra-Romero, G., and Alonzo-Garcia, A. (2021). Analysis of the turbulent flow patterns generated in isotropic porous media composed of aligned or centered cylinders. International Journal of Mechanical Sciences *199*, 106396. https://doi.org/10.1016/j.ijmecsci.2021.106396.

[S11]. Lopes, J.P., and Rodrigues, A.E. (2016). Monolith reactors. In Multiphase Catalytic Reactors (John Wiley & Sons, Ltd), pp. 171–212. https://doi.org/10.1002/9781119248491.ch8.

[S12]. Forchheimer Equation - an overview | ScienceDirect Topics https://www.sciencedirect.com/topics/engineering/forchheimer-equation.

[S13]. Zeitschrift der Vereines Deutscher Ingenieure (1909). (Rudolph Gaertner).

[S14]. Aluminum Oxide | Al2O3 Material Properties https://accuratus.com/alumox.html.

[S15]. Silicon Carbide SiC Material Properties https://accuratus.com/silicar.html.

[S16]. Siliconized SiC Beam | SiSiC Beams https://www.ceramicsrefractories.saint-gobain.com/products/shapes/beams/silit-beams.

[S17]. Fused Silica | SiO2 Material Properties https://accuratus.com/fused.html.

[S18]. Levenspiel, O. (1998). Chemical Reaction Engineering (John Wiley & Sons).

[S19]. Vidal Vázquez, F., Pfeifer, P., Lehtonen, J., Piermartini, P., Simell, P., and Alopaeus, V. (2017). Catalyst Screening and Kinetic Modeling for CO Production by High Pressure and Temperature Reverse Water Gas Shift for Fischer–Tropsch Applications. Ind. Eng. Chem. Res. *56*, 13262–13272. https://doi.org/10.1021/acs.iecr.7b01606.